

ARTICLE TYPE

C/O ratios in self-gravitating protoplanetary discs with dust evolution

Tamara Molyarova,^{1,2} Eduard Vorobyov,^{1,2} and Vitaly Akimkin¹¹Institute of Astronomy, Russian Academy of Sciences, 48 Pyatnitskaya St., Moscow, 119017, Russia²Research Institute of Physics, Southern Federal University, Stachki Ave. 194, Rostov-on-Don 344090, Russia

Author for correspondence: Tamara Molyarova, Email: moliarova@sfnedu.ru.

Abstract

Elemental abundances, particularly the C/O ratio, are seen as a way to connect the composition of planetary atmospheres with planet formation scenario and the disc chemical environment. We model the chemical composition of gas and ices in a self-gravitating disc on timescales of 0.5 Myr since its formation to study the evolution of C/O ratio due to dust dynamics and growth, and phase transitions of the volatile species. We use the thin-disc hydrodynamic code FEOSAD, which includes disc self-gravity, thermal balance, dust evolution and turbulent diffusion, and treats dust as a dynamically different and evolving component interacting with the gas. It also describes freeze-out, sublimation and advection of four most abundant volatile species: H₂O, CO₂, CH₄ and CO. We demonstrate the effect of gas and dust substructures such as spirals and rings on the distribution of volatiles and C/O ratios, including the formation of multiple snowlines of one species, and point out the anticorrelation between dust-to-gas ratio and total C/O ratio emerging due to the contribution of oxygen-rich ice mantles. We identify time and spatial locations where two distinct trigger mechanisms for planet formation are operating and differentiate them by C/O ratio range: wide range of the C/O ratios of 0–1.4 for streaming instability, and a much narrower range 0.3–0.6 for gravitational instability (with the initial value of 0.34). This conclusion is corroborated by observations, showing that transiting exoplanets, which possibly experienced migration through a variety of disc conditions, have significantly larger spread of C/O in comparison with directly imaged exoplanets likely formed in gravitationally unstable outer disk regions. We show that the ice-phase C/O \approx 0.2–0.3 between the CO, CO₂ and CH₄ snowlines corresponds to the composition of the Solar system comets, that represent primordial planetesimals.

Keywords: protoplanetary disc, volatiles, dust evolution**1. Introduction**

The protoplanetary disc matter can be roughly divided into three component: gaseous chemical species, solid dust particles, and icy mantles covering the surface of dust grains. Gas and solid particles become dynamically decoupled, as evolving dust grows and acquires relative velocities leading to the redistribution of elements in the disc and between the phases, and creating the premises for different chemical environments. When planets start to form, their properties, including chemical composition of the atmosphere, are inevitably affected by the location and the mechanism of their formation. This suggests that the origin of (exo)planets might be investigated using their observed chemical composition, and makes understanding the disc chemical evolution vital for creating a consistent planet formation theory.

One of the key parameters that govern the chemical setup of a planetary atmosphere is the relation between the abundances of carbon and oxygen, often referred to as carbon-to-oxygen ratio (hereafter C/O ratio). The variations of C/O ratio in the ice and gas phases at the snowlines of main disc volatiles (CO, CO₂, and H₂O) and the prospects of connecting them to planet formation were discussed in Öberg, Murray-Clay, and Bergin (2011) within a qualitative freeze-out model. Since then, C/O ratio received a lot of attention in this context. It was thoroughly investigated in modelling (see, e.g., Booth et al. 2017; Eistrup, Walsh, and van Dishoeck 2018; Cridland, Eistrup, and van Dishoeck 2019; Cridland et al. 2019; Crid-

land, Bosman, and van Dishoeck 2020; Cridland et al. 2020; Krijt et al. 2020; Turrini et al. 2021; Schneider and Bitsch 2021). The connection of disc chemical composition with C/O in exoplanetary atmospheres was modelled using core accretion model (Thiabaud et al. 2015) and “chain” planet population synthesis model (Mordasini et al. 2016). Paul Mollière et al. (2022) considered a simple formation retrieval pipeline and found that this task requires careful consideration of the model assumptions.

The measurements of molecular abundances in the atmospheres of giant exoplanets obtained by a variety of modern facilities, such as HST, Spitzer, VLTI, JWST, Gemini, indicate a diversity of C/O ratios: from low C/O ratio values (\approx 0.4, below the solar value of 0.54; Benneke et al. 2019; GRAVITY Collaboration et al. 2020; Worthen et al. 2024; Xue et al. 2024) to stellar (\approx 0.5, close to solar; P. Mollière et al. 2020; Zhang et al. 2021; Smith et al. 2024) and close to or above unity (Swain et al. 2009; Madhusudhan et al. 2011). A variety of solar and super-solar C/O ratios is observed in four planets within the HR8799 system (Nasedkin et al. 2024). Chemical composition of the atmospheres of many hot Jupiters indicates high C/O > 1 of the forming material (Moses et al. 2013). There is an observational evidence of young planets in PDS 70 disc accreting the material with C/O > 1 (Facchini et al. 2021). The number of exoplanets with constrained atmospheric C/O ratios grows with large studies of multiple planets such as Changeat et al. (2022), which allows us to make some statistical conclusions. The

population study of C/O ratios in exoplanetary atmospheres reveals that there are two populations with different elemental ratios, which are likely formed in different mechanisms (Hoch *et al.* 2023). Khorshid, Min, and Désert (2023) were able to restrict the formation scenario for WASP-77b based on the measured C/O ratio of the planet (Line *et al.* 2021) and the modelling of planet formation and migration.

Elemental abundances in protoplanetary discs can be constrained from observations (Fedele and Favre 2020), and C/O ratio in the gas can be estimated. Spatially resolved observations can help distinguish between different C/O ratios spectroscopically (Matter, Pignatale, and Lopez 2020). Cleaves *et al.* (2018) report $C/O \approx 0.8$ in the molecular layer of IM Lup disc. ALMA observations of hydrocarbons and sulphur-bearing species indicate $C/O > 1$ in the upper disc layers and in the outer disc in TW Hya and DM Tau (Dutrey *et al.* 2011; Bergin *et al.* 2016; Semenov *et al.* 2018) and for a population of discs in Lupus (Miotello *et al.* 2019). For the nearby discs the solar elemental composition with $C/O \approx 0.54$ is usually expected, thus the observed higher values confirm redistribution of carbon and oxygen in discs. In addition to high C/O in disc atmospheres, there is evidence of both carbon and oxygen depletion from gas (Kama *et al.* 2016; Miotello *et al.* 2019). However, some of heavy oxygen carriers might not be observable, leading to overestimated C/O in disc observations (Walsh, Nomura, and van Dishoeck 2015).

The volatile composition is also used to constrain the origin of bodies in the Solar System. Fraction of CO and CO₂ ices relative to water in cometary comae indicate their formation between the CO and CO₂ snowlines or exterior to the CO snowline (A’Hearn *et al.* 2012; Seligman *et al.* 2022). Abundances of CO and N₂ ices were used to analyse the original location of Pluto and Triton (Mousis, Anderson, *et al.* 2024). Observed elemental abundances were used to constrain the Jupiter formation scenario (Lodders 2004), relying also on abundances of nitrogen (Öberg and Wordsworth 2019; Bosman, Cridland, and Miguel 2019) and chemically inactive species like Ar. However, the model assumptions can lead to different interpretation of the observations: while Öberg and Wordsworth (2019) and Bosman, Cridland, and Miguel (2019) suggest that Jupiter formed outside N₂ snowline (at > 30 au), Ohno and Ueda (2021) consider the concept disc shadow, which allows Jupiter to form near its current location.

Chemical processes other than freeze-out and sublimation at the snowlines can alter the composition of ice and gas as well. Due to gas-phase and surface reactions, snowlines can become important for the redistribution of elements. More detailed chemical modelling shows that the C/O ratio in the gas and in the ice depends also on the initial chemical setup and ionisation by cosmic rays and radioactive nuclei (Eistrup, Walsh, and van Dishoeck 2016, 2018). It directly affects the interpretation of observations. Another essential chemical process is CO depletion from the gas, resulting in its transformation to CO₂ ice (Bosman, Tielens, and van Dishoeck 2018). For example, stellar C/O ratio in the atmosphere of HR 8799e indicates that the planet accreted its material beyond CO snowline (≈ 45 au), but chemical modelling suggests that due to CO depletion,

the C/O in the ice already approaches the stellar ratio beyond CO₂ snowline (≈ 20 au), which is closer to the star (P. Mollière *et al.* 2020).

Another key process affecting the elemental ratio is dust drift, which leads to spatial segregation between the chemical constituents of the gas and the grains covered with ice. The distribution of CO in the gas and ice phases was studied within dynamical models of dust evolution (Stammler *et al.* 2017; Krijt *et al.* 2018). Even without chemical processes, dust evolution and dynamics can substantially alter C/O ratio in the atmospheres of forming planets (Booth *et al.* 2017). Some models combine chemical reactions treatment with dust evolution and transport, usually within 1D viscous models. Dust transport can have a strong effect on the abundances of volatiles in the inner disc regions (Bosman, Tielens, and van Dishoeck 2018). However, for discs with low turbulence and high cosmic ray ionisation rate, C/O ratio is rather defined by chemical evolution (Booth and Ilee 2019).

In our previous work (Molyarova *et al.* 2021) we showed that the volatile species tend to concentrate around their snowlines both in the gas and more notably on the dust surface. This accumulation was found to be caused by effective transport of volatiles through the snowlines by azimuthal variations in the gas and dust radial and angular velocity, an effect that cannot be captured in 1D viscous disc models. Such accumulation should immediately affect the local C/O ratio, which suggests the connection between the snowlines of various volatiles and the formation of planets with altered C/O in their atmospheres. In this work, we follow the distribution of the main volatile species in the disc to investigate the distribution of C/O ratio in gas and ice in a 2D thin-disc hydrodynamic model. We study the effect of dust growth and dynamics on the elemental ratios and consider the role of the initial mass of the collapsing core on the distribution of volatiles.

The paper is organised as follows. The main features of the used FEOSAD model are described in Section 2, with the details of the treatment of the volatiles given in Section 2.3. In Section 3 we describe the results of the simulations, focusing on distribution of the volatiles in Section 3.2, the C/O ratios in Section 3.3, and their evolution in Section 3.4. In Section 4, we discuss the implications of our results in the context of planet formation via different mechanisms. The main conclusions are listed in Section 5.

2. Model

We use the global model of protoplanetary disc formation FEOSAD (Vorobyov *et al.* 2018), which includes disc self-gravity, dust evolution and interaction with gas (including backreaction of dust on gas), turbulent viscosity, adiabatic and radiative cooling and heating. It describes the formation of a protostar and a protoplanetary disc from a collapsing cloud in a 2D thin-disc approach. The model also includes freeze-out of main volatile species as in Molyarova *et al.* (2021), with the feedback from ice mantles on dust evolution via fragmentation velocity. Here we summarise the key characteristics of the model, more details can be found in the previous works (Vorobyov

et al. 2018; Molyarova et al. 2021; Kadam, Vorobyov, and Basu 2022). The main difference from our previous study in Molyarova et al. (2021) is that here we consider the formation of dead zones via variable α -parameter of Shakura and Sunyaev and also include turbulent diffusion.

2.1 Gas evolution

For the gas component, the hydrodynamic equations for mass, momentum, and internal energy conservation are the following

$$\frac{\partial \Sigma_{\text{g}}}{\partial t} + \nabla \cdot (\Sigma_{\text{g}} \boldsymbol{\nu}) = 0, \quad (1)$$

$$\begin{aligned} \frac{\partial}{\partial t} (\Sigma_{\text{g}} \boldsymbol{\nu}) + [\nabla \cdot (\Sigma_{\text{g}} \boldsymbol{\nu} \otimes \boldsymbol{\nu})] &= -\nabla \mathcal{P} + \Sigma_{\text{g}} \boldsymbol{g} + \\ + \nabla \cdot \boldsymbol{\Pi} - \Sigma_{\text{d,gr}} \boldsymbol{f}, \end{aligned} \quad (2)$$

$$\frac{\partial e}{\partial t} + \nabla \cdot (e \boldsymbol{\nu}) = -\mathcal{P}(\nabla \cdot \boldsymbol{\nu}) - \Lambda + \Gamma + \nabla \boldsymbol{\nu} : \boldsymbol{\Pi}, \quad (3)$$

where subscripts p and p' denote the planar components (r, ϕ) in polar coordinates, Σ_{g} is the gas mass surface density, e is the internal energy per surface area, \mathcal{P} is the vertically integrated gas pressure calculated via the ideal equation of state as $\mathcal{P} = (\gamma - 1)e$ with $\gamma = 7/5$, \boldsymbol{f} is the friction force between gas and dust, $\boldsymbol{\nu} = \nu_r \hat{\boldsymbol{r}} + \nu_\phi \hat{\boldsymbol{\phi}}$ is the gas velocity in the disc plane, and $\nabla = \hat{\boldsymbol{r}} \partial / \partial r + \hat{\boldsymbol{\phi}} r^{-1} \partial / \partial \phi$ is the gradient along the planar coordinates of the disc. The gravitational acceleration in the disc plane, $\boldsymbol{g} = g_r \hat{\boldsymbol{r}} + g_\phi \hat{\boldsymbol{\phi}}$, includes the gravity of the central protostar when formed and takes into account disc self-gravity of both gas and dust found by solving the Poisson integral (Binney and Tremaine 1987).

The consideration of time-dependent energy balance (Eq. (3)) allows us to accurately calculate the midplane temperature T_{mp} and is particularly important to describe the phase state of the volatiles and the level of turbulent viscosity. The terms Λ and Γ describe the rates of dust cooling and heating, respectively, by stellar and background irradiation. They are calculated based on the analytical solution of the radiation transfer equations in the vertical direction (Dong et al. 2016; Vorobyov et al. 2018)

$$\Lambda = \frac{8\tau_{\text{p}} \sigma T_{\text{mp}}^4}{1 + 2\tau_{\text{p}} + \frac{3}{2}\tau_{\text{p}}\tau_{\text{R}}}, \quad \Gamma = \frac{8\tau_{\text{p}} \sigma T_{\text{irr}}^4}{1 + 2\tau_{\text{p}} + \frac{3}{2}\tau_{\text{p}}\tau_{\text{R}}}. \quad (4)$$

Here, σ is the Stefan-Boltzmann constant, τ_{p} and τ_{R} are the Planck and Rosseland mean optical depths to the disc midplane, calculated as $\tau = \kappa \Sigma_{\text{dust}}$ from Planck and Rosseland mean opacities κ_{p} and κ_{R} (Semenov et al. 2003) and total dust surface density Σ_{dust} . Gas and dust temperatures are assumed to be equal, and the midplane temperature is linked with gas pressure as $T_{\text{mp}} = \mathcal{P} \mu / \mathcal{R} \Sigma_{\text{g}}$, where $\mu = 2.3$ is the mean molecular weight of the gas, and \mathcal{R} is the universal gas constant. The irradiation temperature at the disc surface T_{irr} is determined by both stellar and background irradiation. Stellar irradiation includes the luminosity from the photosphere of the protostar

and accretion luminosity. The background radiation is assumed as a black body with the temperature of 15 K. For more details on the irradiation we refer to Vorobyov et al. (2018).

Turbulent viscosity is described using the common α -parameter approach of Shakura and Sunyaev (1973). It is taken into account via the viscous stress tensor $\boldsymbol{\Pi}$ (see Vorobyov and Basu 2010, for explicit expressions for the components of the terms with $\boldsymbol{\Pi}$). The magnitude of kinematic viscosity is $\nu = \alpha c_s H$, where c_s is the sound speed and H is the vertical scale height of the gas disc calculated using an assumption of local hydrostatic equilibrium of a self-gravitating disc (see Vorobyov and Basu 2010, Appendix A). Here, we use the adaptive α approach implying accretion through a layered disc (Gammie 1996; Armitage, Livio, and Pringle 2001; Kadam, Vorobyov, and Basu 2022). Turbulence is assumed to be generated by magneto-rotational instability (MRI) which only develops in layers of the disc where the ionisation level is high enough. The MRI-active layer is characterised by its surface density Σ_{MRI} and relatively high value of turbulent viscosity $\alpha_{\text{MRI}} = 10^{-3}$. As thermal and photo-ionisation are not efficient enough for the relatively cold and dense matter in the disc at >0.5 au, the main process determining the thickness of the MRI-active layer is ionisation by cosmic rays. It is assumed to be constant $\Sigma_{\text{MRI}} = 100 \text{ g cm}^{-2}$, which is the typical depth of Galactic cosmic rays penetration in the ISM (Umebayashi and Nakano 1981) and in protoplanetary discs (Padovani, Galli, and Glassgold 2009). The dead zone is characterised by surface density from the midplane $\Sigma_{\text{dz}} = \Sigma_{\text{g}}/2 - \Sigma_{\text{MRI}}$ with residual turbulence α_{dz} . The turbulence in this layer is only hydrodynamic turbulence driven by the Maxwell stress in the active layer, and small value $\alpha_{\text{dz}} = 10^{-5}$ is adopted (Okuzumi and Hirose 2011). However, if local temperature exceeds the critical value of 1300 K, thermal ionisation becomes possible, the MRI develops and the dead zone is no longer dead, in which case $\alpha_{\text{dz}} = 10^{-1}$ (Zhu et al. 2010; Kadam et al. 2019). This value is higher than α_{MRI} in the outer disc due to the different ionisation processes and local conditions. In the outer disc, the MRI can be suppressed by non-ideal magneto-hydrodynamic (MHD) effects such as ambipolar diffusion and Ohmic resistivity (Bai and Stone 2013; Gressel et al. 2015). In the dead zone in the inner disc, α can reach higher values when the MRI is triggered by thermal ionisation, as shown by 3D MHD simulations (Zhu, Jiang, and Stone 2020). The adopted parameterization makes use of an effective parameter α_{eff} , which at any given location is calculated as

$$\alpha_{\text{eff}} = \frac{\Sigma_{\text{MRI}} \alpha_{\text{MRI}} + \Sigma_{\text{dz}} \alpha_{\text{dz}}}{\Sigma_{\text{MRI}} + \Sigma_{\text{dz}}}, \quad \alpha_{\text{dz}} = \begin{cases} 10^{-5}, & \text{if } T_{\text{mp}} < 1300\text{K}; \\ 10^{-1}, & \text{if } T_{\text{mp}} \geq 1300\text{K}. \end{cases} \quad (5)$$

2.2 Dust evolution

Dust is described as consisting of two components: small grains that are dynamically coupled to the gas, with the mass surface density $\Sigma_{\text{d,sm}}$, and grown grains with the mass surface density $\Sigma_{\text{d,gr}}$ that can move relative to the gas and change in size. The total dust surface density necessary for the calculation

of the optical depths for Eq. (4) is $\Sigma_{\text{dust}} = (\Sigma_{\text{d,gr}} + \Sigma_{\text{d,sm}})/2$. The factor 1/2 appears as the optical depths is calculated to the midplane. Each dust population has a power-law size distribution $f(a) = dN/da = Ca^{-p}$ with a normalisation constant C and a fixed exponent $p = 3.5$. Small dust has sizes between $a_{\text{min}} = 5 \times 10^{-7}$ cm and $a_* = 10^{-4}$ cm, grown dust has sizes between a_* and a_{max} , which can vary due to dust coagulation and fragmentation. Dynamics of these dust components follows the continuity and momentum equations

$$\frac{\partial \Sigma_{\text{d,sm}}}{\partial t} + \nabla \cdot (\Sigma_{\text{d,sm}} \mathbf{v}) = -S(a_{\text{max}}) + \nabla \cdot \left(D \Sigma_{\text{g}} \nabla \left(\frac{\Sigma_{\text{d,sm}}}{\Sigma_{\text{g}}} \right) \right), \quad (6)$$

$$\frac{\partial \Sigma_{\text{d,gr}}}{\partial t} + \nabla \cdot (\Sigma_{\text{d,gr}} \mathbf{u}) = S(a_{\text{max}}) + \nabla \cdot \left(D \Sigma_{\text{g}} \nabla \left(\frac{\Sigma_{\text{d,gr}}}{\Sigma_{\text{g}}} \right) \right), \quad (7)$$

$$\begin{aligned} \frac{\partial}{\partial t} (\Sigma_{\text{d,gr}} \mathbf{u}) + \left[\nabla \cdot (\Sigma_{\text{d,gr}} \mathbf{u} \otimes \mathbf{u}) \right] &= \Sigma_{\text{d,gr}} \mathbf{g} + \\ &+ \Sigma_{\text{d,gr}} \mathbf{f} + S(a_{\text{max}}) \mathbf{v}, \end{aligned} \quad (8)$$

where \mathbf{u} is the grown dust velocity. The term $S(a_{\text{max}})$ is responsible for the exchange of matter between the dust populations, as dust is converted from the small to grown component due to coagulation and back due to fragmentation. The details of the dust evolution model are presented in Vorobyov et al. (2018). The last term in Eqs. (6) and (7) is responsible for dust turbulent diffusion, similar to Vorobyov, Elbakyan, et al. (2020). The coefficient of turbulent diffusion D is related to the kinematic viscosity ν as $D = \nu/(1 + \text{St}^2)$ (Birnstiel 2023). Diffusion affects dust grains along with their ice mantles, as well as the gas-phase species (see Section 2.3).

The innermost regions of the disc are challenging to simulate explicitly due to the Courant criterion: in the highly dynamic inner regions (fraction of au) the timescales are so short that the code demands very small time step in order to preserve stability. Therefore, the inner regions are represented by a sink cell, with a carefully chosen inflow-outflow boundary condition at the sink cell and a parametric description of the accretion onto the star (see Vorobyov et al. 2018, for details). In the simulations presented below, the radius of the sink cell is 0.62 au.

We consider two disc models with different initial mass of the collapsing cloud, 0.66 and 1 M_{\odot} . We note that about 10% of the gas mass that crosses the sink cell is assumed to be evacuated by jets and outflows, and the other 90% lands on to the star. A small amount of mass remains in the envelope by the end of simulations. In both models, the initial gas temperature $T_{\text{init}} = 15$ K and the ratio of rotational to gravitational energy $\beta = 0.28\%$. The simulations start from the collapse of a molecular cloud, with only small dust grains. The simulation continues until the age of the system becomes equal to 0.5 Myr. Masses of the central protostar and the disc by the end of simulation are $M_{\star} = 0.4 M_{\odot}$ and $M_{\text{disc}} = 0.22 M_{\odot}$ in model M1 and $M_{\star} = 0.58 M_{\odot}$ and $M_{\text{disc}} = 0.35 M_{\odot}$ in model M2. The disc masses are around 0.5 stellar masses, which makes them essentially self-gravitating.

A number of recent studies develop the idea that the mass infall from the ambient ISM continues during the lifetime of the disc, including the Class II stage (Padoan et al. 2024; Pelkonen et al. 2024; Winter, Benisty, and Andrews 2024). Such models describe a Bondi–Hoyle accretion regime and are in good agreement with the observed properties of the disc population, such as accretion rates, masses and sizes. This input of matter can play an important role in disc evolution and planet formation process (Vorobyov, Lin, and Guedel 2015; Vorobyov et al. 2016). In the FEOSAD model, the mass infall to the disc can be accounted for (Vorobyov, Lin, and Guedel 2015; Vorobyov et al. 2016), but in the present simulation this effect is not included. The mass infall from the envelope continues until the cloud is depleted of matter. Because of the thin-disc geometry, the gravitational contraction of the cloud proceeds in the plane of the disc. The matter is landing on the disc outer edge and is transported towards the star by the combined action of gravitational and viscous torques. The infall on the disc inner regions is therefore neglected. This is a reasonable approximation, considering that most of the matter and angular momentum in a three-dimensional cloud is located at relatively large polar angles and a flared outer edge of the disc intercepts most of them (see, e.g., Visser et al. 2009, Figure 1). In our modelling, we do not consider the continuous Bondi–Hoyle accretion and concentrate on the internal disc processes.

2.3 Evolution of volatiles

We follow the evolution of four main volatile species: H_2O , CO_2 , CO and CH_4 . These are the most abundant carbon- and oxygen-bearing ices observed in protostellar cores (Karin I. Öberg et al. 2011). In the model, each of these species can be present in three states: in the gas, in the ice on the surface of small dust, and in the ice on the surface of grown dust. Each species s is described by its surface density in the gas Σ_s^{gas} , on small dust Σ_s^{sm} , and on grown dust Σ_s^{gr} . Their distributions in the disc can change through three main processes: advection together with the corresponding component (gas or small/grown dust); exchange of mantles between dust populations due to grain collisions; phase transitions, including adsorption from gas to dust, and thermal and photo-desorption. Initially, all ices are on small grains and no volatiles present in the gas. The treatment of volatiles is adopted from Molyarova et al. (2021), who describe the models in more details. Here we recap main features of the chemical model.

Our chemical model only describes phase transitions, i.e. adsorption and desorption, which includes thermal desorption and photo-desorption by interstellar UV radiation. These reactions were shown to be the most important for gas-phase abundances of most species (Ilee et al. 2011). Due to high computational costs, no other chemical processes, either gas-phase or surface reactions are included, although they also may have significant effect on the composition of both ice and gas (Semenov and Wiebe 2011). The chemical evolution of the surface densities of volatile species is calculated from the

system of equations

$$\frac{\partial \Sigma_s^{\text{gas}}}{\partial t} + \nabla \cdot (\Sigma_s^{\text{gas}} \boldsymbol{\nu}) - \nabla \cdot \left(D \Sigma_g \nabla \left(\frac{\Sigma_s^{\text{gas}}}{\Sigma_g} \right) \right) = -\lambda_s \Sigma_s^{\text{gas}} + \eta_s^{\text{sm}} + \eta_s^{\text{gr}}, \quad (9)$$

$$\frac{\partial \Sigma_s^{\text{sm}}}{\partial t} + \nabla \cdot (\Sigma_s^{\text{sm}} \boldsymbol{\nu}) - \nabla \cdot \left(D \Sigma_g \nabla \left(\frac{\Sigma_s^{\text{sm}}}{\Sigma_g} \right) \right) = \lambda_s^{\text{sm}} \Sigma_s^{\text{gas}} - \eta_s^{\text{sm}}, \quad (10)$$

$$\frac{\partial \Sigma_s^{\text{gr}}}{\partial t} + \nabla \cdot (\Sigma_s^{\text{gr}} \boldsymbol{u}) - \nabla \cdot \left(D \Sigma_g \nabla \left(\frac{\Sigma_s^{\text{gr}}}{\Sigma_g} \right) \right) = \lambda_s^{\text{gr}} \Sigma_s^{\text{gas}} - \eta_s^{\text{gr}}, \quad (11)$$

where the mass rate coefficients per disc unit area of adsorption λ_s and desorption η_s for the species s are calculated for local conditions at every hydrodynamic step, separately for small and grown dust populations. Eqs. (9)–(11) are solved in two steps: first, the right-hand side is considered without the advection term. The case of pure adsorption/desorption represented by the right-hand side of the equation can be solved analytically (see Appendix A in Molyarova et al. 2021). This is done at every hydrodynamic step, before the dust growth step, when ices on small and grown grains are redistributed proportionally to mass exchange between the dust populations. This is followed by a transport step, when the surface densities of the volatiles are changed according to the fluxes of their respective gas or dust components between the cells. Restricting chemical processes to only adsorption and desorption allows the chemical step to be calculated fast, which is very important for computationally demanding hydrodynamic simulations.

For each dust population, the desorption rate is a sum of thermal desorption and photo-desorption $\eta = \eta_{\text{td}} + \eta_{\text{pd}}$ (the indices “sm” and “gr” are omitted for convenience). We operate under the assumption of zeroth-order desorption, i.e. the desorption rate does not depend on the present amount of ice (Σ_s^{sm} or Σ_s^{gr}). It implies that only the upper layers of the ice mantle are able to sublimate, which is a more appropriate approach for thick mantles. This assumption better describes desorption of CO and H₂O in temperature programmed desorption (TPD) experiments (Fraser et al. 2001; K. I. Öberg et al. 2005; Bisschop et al. 2006) than first-order desorption, which is more suitable for thin mantles of several monolayers. The rate of thermal desorption is calculated as

$$\eta_{\text{td}} = \tilde{\sigma}_{\text{tot}} N_{\text{ss}} \mu_s m_p \sqrt{\frac{2N_{\text{ss}} E_b k_B}{\pi^2 \mu_s m_p}} \exp\left(-\frac{E_b}{T_{\text{mp}}}\right), \quad (12)$$

where $N_{\text{ss}} = 10^{15} \text{ cm}^{-2}$ is the surface density of binding sites (Cuppen et al. 2017), E_b (K) is the binding energy of the species to the surface, μ_s is the species molecular mass, m_p is atomic mass unit, k_B is the Boltzmann constant. We follow Hasegawa and Herbst (1993) and use binding energy to calculate the pre-exponential factor in Eq. (12), the same way it was done in Molyarova et al. (2021). However, this approach was recently demonstrated by Minissale et al. (2022) to underestimate the pre-exponential factor by a few orders of magnitude,

as it does not account for the rotational part of the partition functions of desorbing molecules. Total surface area of dust grains (small or grown) per disc unit area $\tilde{\sigma}_{\text{tot}}$ ($\text{cm}^2 \text{ cm}^{-2}$) is calculated for the adopted power-law size distribution with $p = 3.5$ as

$$\tilde{\sigma}_{\text{tot}}^{\text{sm}} = \frac{3 \Sigma_{\text{d,sm}}}{\rho_s \sqrt{a_{\text{min}} a_*}}, \quad (13)$$

$$\tilde{\sigma}_{\text{tot}}^{\text{gr}} = \frac{3 \Sigma_{\text{d,gr}}}{\rho_s \sqrt{a_* a_{\text{max}}}}. \quad (14)$$

Here, $\rho_s = 3 \text{ g cm}^{-3}$ is the material density of silicate cores of the dust grains.

The model includes photodesorption of volatiles by interstellar irradiation, which is mostly relevant in the outer disc regions with lower optical depth. We do not consider the UV radiation field produced by the star and the accretion region as a source of photodesorption, assuming that they do not reach disc midplane due to high optical depth. The photo-desorption rate is calculated as

$$\eta_{\text{pd}} = \tilde{\sigma}_{\text{tot}} \mu_{\text{sp}} m_p Y F_{\text{UV}}. \quad (15)$$

where $F_{\text{UV}} = F_0^{\text{UV}} G_{\text{UV}}$ (photons $\text{cm}^{-2} \text{ s}^{-1}$) is the UV photon flux expressed in the units of standard UV field and $Y = 3.5 \times 10^{-3} + 0.13 \exp(-336\text{K}/T_{\text{mp}})$ (mol photon⁻¹) is the photodesorption yield adopted from Westley et al. (1995) for water ice. The intensity of the interstellar UV radiation field with $G_0 = 1$ is $F_0^{\text{UV}} = 4.63 \times 10^7 \text{ photon cm}^{-2} \text{ s}^{-1}$ (Draine 1978). We assume that the disc situated in a star-forming region is illuminated by a slightly elevated unattenuated UV field with $G_{\text{env}} = 5.5 G_0$. For the disc midplane, which is illuminated from above and below, this field scales with the UV optical depth τ_{UV} towards the disc midplane as

$$G_{\text{UV}} = 0.5 G_{\text{env}} e^{-\tau_{\text{UV}}}. \quad (16)$$

The optical depth can be calculated as $\tau_{\text{UV}} = 0.5(\kappa_{\text{sm}} \Sigma_{\text{d,sm}} + \kappa_{\text{gr}} \Sigma_{\text{d,gr}})$, where $\kappa_{\text{sm}} = 10^4 \text{ cm}^2 \text{ g}^{-1}$, $\kappa_{\text{gr}} = 2 \times 10^2 \text{ cm}^2 \text{ g}^{-1}$ are typical values of absorption coefficients in the UV for small and grown grains (Pavlyuchenkov et al. 2019, Fig. 1).

We calculate the adsorption rate λ following Brown and Charnley (1990). It is proportional to the total cross-section of dust grains per unit volume, which can be obtained from the total surface area of dust grains per unit disc surface $\tilde{\sigma}_{\text{tot}}$. To change the normalisation to the 2D case, $\tilde{\sigma}_{\text{tot}}$ needs to be multiplied by $1/2H$. Another factor of $1/4$ follows from the difference between cross-section and surface area of a sphere. As a result, the adsorption rate is calculated as

$$\lambda = \frac{\tilde{\sigma}_{\text{tot}}}{8H} \sqrt{\frac{8k_B T_{\text{mp}}}{\pi \mu_{\text{sp}} m_p}}. \quad (17)$$

A more detailed derivation of rate coefficients for adsorption and desorption is presented in Section 2.3 of Molyarova et al. (2021).

Table 1. Binding energies, molecular weights, and initial abundances for the considered volatiles adopted in the modelling. Initial abundances of the species f_s are shown relative to number density of water molecules in ice phase, and $\Sigma_s^{\text{sm}}/\Sigma_g^{\text{init}}$ is the corresponding initial mass fraction of the ices relative to gas surface density.

Species	E_b , K	μ_s , amu	f_s , %	$\Sigma_s^{\text{sm}}/\Sigma_g^{\text{init}}$
H ₂ O	5770	18	100	3.90×10^{-4}
CO ₂	2360	44	29	2.77×10^{-4}
CO	850	28	29	1.76×10^{-4}
CH ₄	1100	16	5	1.74×10^{-5}

Table 1 summarises the molecular parameters used in both models in this work. Binding energies for H₂O, CO₂, and CO are based on the experimental data from Cuppen *et al.* (2017) for desorption from crystalline water ice. The binding energy for methane is taken from Aikawa *et al.* (1996). The values of the initial abundances relative to water f_s are based on the observations of ices in protostellar cores around the low-mass protostars (Karin I. Öberg *et al.* 2011). They are transformed to the mass fraction relative to gas assuming the water abundance of 5×10^{-5} relative to gas number density. Total initial mass of ices comprises $\approx 8.5\%$ of the total mass of refractory grain cores. This is relatively low compared to the estimates suggesting comparable masses of ices and refractories in the discs (Pontoppidan *et al.* 2014). However, the lower fraction of ices is more suitable in our approach, that suggests that ice mantles do not change mass and radius of dust grains (Molyarova *et al.* 2021). As we are mostly interested in the elemental ratios and relative abundances of the considered ices, lower ice fraction is an appropriate simplification. However, we note that dust dynamics can lead to accumulation of ices and ice mantles exceeding masses of silicate cores in some disc regions, as was shown previously in Molyarova *et al.* (2021).

Ice mantles also provide feedback on dust evolution. The model includes the effect of ices on fragmentation velocity v_{frag} , which is the the maximum collision velocity leading to sticking instead of fragmentation. According to laboratory experiments, icy grains have higher v_{frag} than bare silicate grains by an order of magnitude (Wada *et al.* 2009; Gundlach and Blum 2015). In Molyarova *et al.* (2021) we used the values of fragmentation velocity $v_{\text{frag}} = 1.5$ and 15 m s^{-1} for bare and icy grains, correspondingly. Here we follow Okuzumi and Tazaki (2019) and adopt lower values of $v_{\text{frag}} = 0.5$ and 5 m s^{-1} , which are more relevant for grains consisting of μm -sized monomers. These lower values of v_{frag} will lead to higher importance of fragmentation compared to Molyarova *et al.* (2021). To determine if a dust grain should be considered icy or bare, we compare the local total surface density of all ices on grown dust divided by $\Sigma_{\text{d,gr}}$ with the threshold value K , which is calculated as

$$K = \frac{3a_{\text{ml}}\rho_{\text{ice}}}{\sqrt{a_*a_{\text{max}}}\rho_s}, \quad (18)$$

i.e., an icy grain must have at least one monolayer of ice. Here, a_{ml} is the thickness of the ice monolayer estimated as the size

of a water molecule $3 \times 10^{-8} \text{ cm}$. The material density of ice $\rho_{\text{ice}} = 1 \text{ g cm}^{-3}$ and the mean radius of a grown grain is calculated as $\sqrt{a_*a_{\text{max}}}$ for the power-law distribution with $p = 3.5$.

3. Results

To understand the distribution of the species, we first need to consider the global evolution of the disc and its structure. The distribution of volatiles and the C/O ratio is very sensitive to gas and dust substructures appearing in the disc. Variations in temperature and pressure lead to the complex shape and temporal evolution of the snowlines. The dependence of dust fragmentation velocity on the presence of ice mantles implies the feedback from the volatiles on dust and (through back-reaction) on gas.

Our modelling starts with the gravitational collapse of a flattened, slowly rotating molecular cloud. The protoplanetary disc is formed after the formation of the protostar, when the in-spiraling layers of the contracting cloud hit the centrifugal barrier near the inner edge of the sink cell, at a time instance depending on the initial core mass. The disc and the protostar are formed ≈ 53 kyr after the beginning of the cloud collapse in model M1 and at ≈ 78 kyr in model M2. If not stated otherwise, times are specified counting from the beginning of the simulation, *e.g.* the 100 kyr time instance for model M1 refers to a ≈ 50 kyr old disc, as the first stage includes cloud collapse as well.

An important characteristic of young stellar objects is their variable accretion rate. Our modelling produces accretion bursts with the magnitude of $\sim 100 L_{\odot}$ occurring every $\sim 10^4$ years during the first hundred thousands years of disc evolution. These burst parameters are in line with the episodic accretion scenario (Hartmann and Kenyon 1985) and resemble the observed phenomenon of FU Ori type stars (see Audard *et al.* 2014, for a review). The luminosity outbursts heat up the disc and typically shift the snowlines further away from the star. Although this effect is temporary, it can be reflected in the distributions of the volatiles, and leave long-term imprints in the observed dust properties (Vorobyov *et al.* 2022). The detailed analysis of the effect of such outbursts on the distribution of the elements is worthy of a separate study and lies beyond the scope of this paper.

3.1 Dust and gas structures

During the first hundred thousands years of evolution, protoplanetary discs change from highly asymmetric and dynamic objects to nearly axisymmetric and slowly evolving structures. Figure 1 shows the examples of different gas and dust substructures that are present in the disc at different stages. The snapshots are shown for model M1, they include a young disc (160 kyr), an intermediate state (350 kyr), and a more evolved and axisymmetric disc (490 kyr). Each of the selected time instances represent some characteristic morphological features addressed below. In model M2, similar structures appear, although sometimes at different evolution times. In this subsection, we consider model M1 as an example and discuss

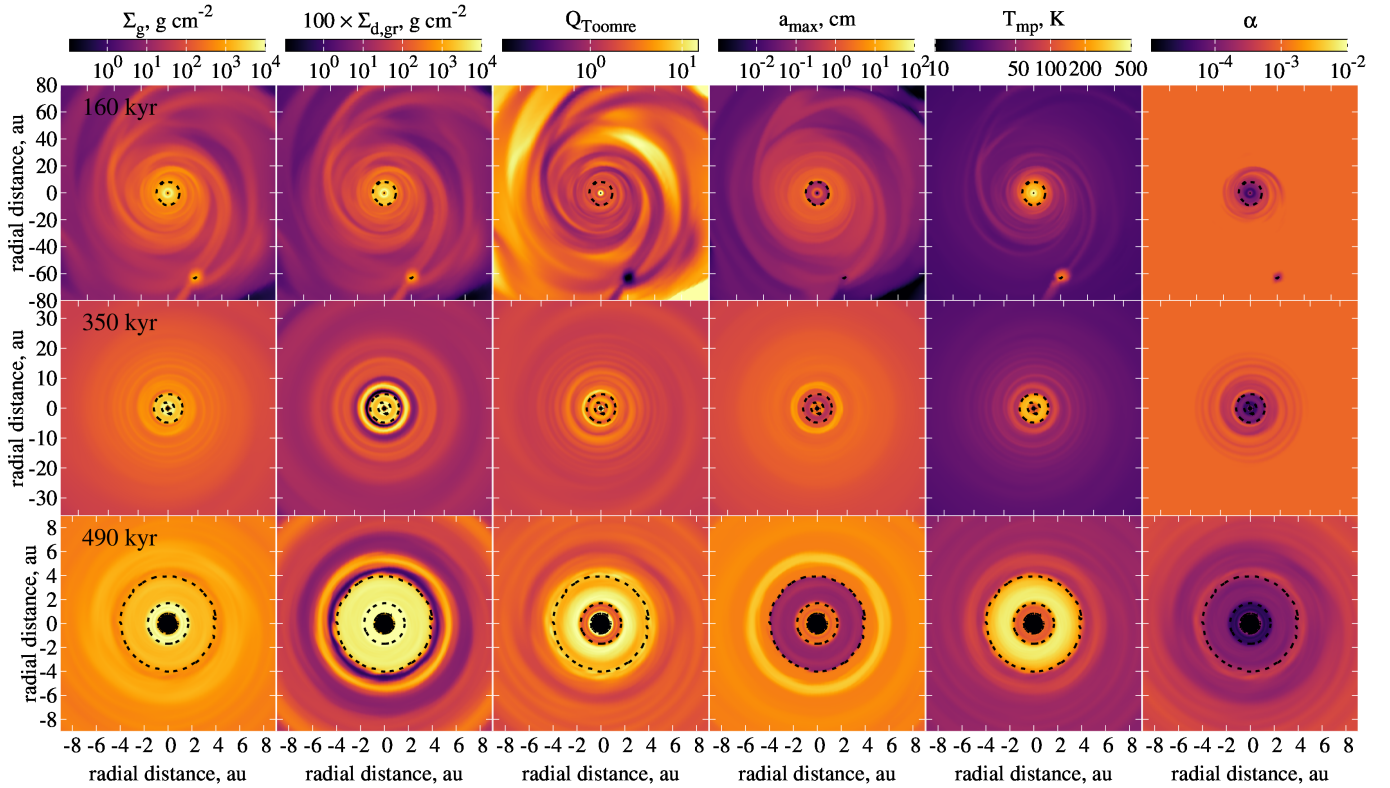


Figure 1. Surface density of gas and grown dust, Toomre Q -parameter, maximum dust radius, temperature and viscous α -parameter in model M1 at selected time moments: 160 kyr, 80×80 au; 350 kyr, 35×35 au; 490 kyr, 9×9 au. The contours indicate the position of the water snowline. Note that at the panels with multiple water snowlines, water is frozen outside the outer line and inside an inner dust ring at $1 - 2$ au.

these features, highlighting the properties of dust and gas substructures that are most relevant for the distribution of the volatiles.

The earliest phases of disc evolution are characterised by a large-scale spiral structure in both dust and gas, as well as episodic appearance of clumps. They are the result of gravitational instability (GI) in a massive disc, as in our modelling, the disc mass comprises more than 0.1 of the stellar mass, which is roughly a threshold of the disc stability against GI (Vorobyov 2013; Kratter and Lodato 2016). This is illustrated by the Toomre Q -parameter (Toomre 1964) in the third column of Figure 1: inside the spirals and the clump $Q < 1$, which indicates the dominance of self-gravity over Keplerian shear and gas density. The spiral structures become less prominent with time as the disc loses mass and the Q -parameter increases. However, spirals persist in the model throughout the disc evolution up to 0.5 Myr. For example, at 350 kyr, a very tight spiral is present in the gas, starting at the gas and dust ring at ≈ 10 au. At 490 kyr, the spiral pattern is weak and exists at > 10 au distances, which are not displayed in Figure 1.

One- or two-armed grand design spirals are common 100 – 200 kyr after the disc formation in the models. The analogues of such spirals in the observed young protoplanetary discs around low-mass stars are found, for example, in Elias 2-27 or WaOph 6 (Pérez et al. 2016; Huang, Andrews, Pérez, et al. 2018). It is not yet clear if the observed spirals are the result of GI or caused by a perturbation from a companion

planet or a (sub)stellar object (Meru et al. 2017; Brown-Sevilla et al. 2021). A spiral with multiple clumps produced by GI was recently observed in the disc around a FUor V960 Mon (Weber et al. 2023).

Another important feature of gas and dust spatial distributions is ring-like structures at various scales. The system of rings starts to form as early as 100 kyr, and develops to the high-contrast multiple ring structure (1 – 3 orders of magnitude difference between surface densities in rings and gaps), which is evident in the middle and bottom rows of Figure 1. While gas rings are also common, the annual structures are more prominent in the dust surface density, as well as in dust size. Some of the dust rings correspond spatially to the gas rings, while others are barely reflected in the gas distribution. Overall, the difference between the gas and dust structures develops with time, as the result of dust growth and drift (Testi et al. 2014). Only some particular substructures, such as the ring between $1 - 2$ au, are present in the distributions of both gas and dust components.

Another location where prominent rings form in both dust and gas is the water snowline. Here, the water snowline is defined as the location in the disc midplane where the amount of water in the gas equals to its amount in the ice (on both dust populations). There are multiple locations in the disc where this happens. Water is frozen in most of the disc beyond $5 - 10$ au, and we will refer to the furthest snowline dividing these outer frozen region from the inner one with the gas-phase water

as a primary snowline. Generally, the primary snowline is roughly circular, but it can have asymmetries due to the spiral structure and an additional snowline may appear, e.g., around a gravitationally bound clump (upper rows in Figure 1). Besides, at ≈ 260 kyr, another region rich in water ice appears in the inner disc, creating a pattern of double or triple water snowline at later times (middle and lower rows in Figure 1). We will refer to these inner additional snowlines as the secondary snowlines. They circumscribe a cold and dense gas-dust ring that forms at 1 – 2 au. As the disc cools down with time, the primary snowline position moves from ≈ 10 au distance at 160 kyr, to ≈ 6 au at 350 kyr and ≈ 4 au at 490 kyr.

Snowlines are known to be associated with the enhancement of dust and volatiles (Stevenson and Lunine 1988; Cuzzi and Zahnle 2004; Drażkowska and Alibert 2017; Molyarova *et al.* 2021). Dust enhancement was also shown to affect the distribution of gas and its accretion rate through the disc (Gárate *et al.* 2020) by means of dust back reaction, which is also accounted for in our modelling. In our models, an about 2 au wide dust ring is formed at the inner edge of the water snowline (at ≈ 10 au) as soon as 50 kyr after the disc formation. Grown dust grains drifting towards the star through the snowline lose their mantles, their fragmentation velocity drops, rendering them more vulnerable to fragmentation. Consequently, the grain maximum size a_{\max} decreases, their drift towards the star slows down, which leads to the accumulation of grown dust, as well as small dust as a product of fragmentation. Increase of total dust density also leads to less efficient cooling and results in higher temperature inside the snowline (see the right panels in Figure 1). Later, at times > 200 kyr, several additional rings form outside the water snowline at distances up to 100 au, the most notable one being 1 – 2 au exterior to the primary snowline. Dust is trapped inside the gas pressure maxima in these rings, which is a self-supporting phenomenon as the temperature also increases inside the dust ring due to high optical depth.

These rings are worthy of attention in the context of possible planet formation. Dust surface density and size are higher in the rings, with a_{\max} reaching centimetres, dust-to-gas ratio up to 0.1 – 0.2, and Stokes number up to 0.05 – 0.1. This could ease the development of the streaming instability, which typically requires pebble-size grains with $St \gtrsim 0.01$ and dust-to-gas ratio $\gtrsim 0.02$ (Carrera, Johansen, and Davies 2015). Multiple ring-like structures are commonly observed in protoplanetary discs at a range of ages and display a variety of examples, with different widths, contrasts and numbers of rings (Huang, Andrews, Dullemond, *et al.* 2018, and many others). However, to directly compare the ring structures in the simulated dust surface density with the observed dust emission, require radiative transfer modelling is needed. Some of the observed ring structures could be produced by radial variation in dust size even in the absence of gaps in dust surface density (Akimkin *et al.* 2020).

The most prominent dust rings are located in the vicinity of the water snowline: the ring outside the primary snowline at 5 – 8 au (depending on the time) and the ring at 1 – 2 au, inside the primary snowline, which at later times also contains water

ice and additional snowlines. The main effect of the snowlines is the change in fragmentation velocity between mantled and non-mantled grains: dust size sharply decreases by ≈ 2 orders of magnitude for the latter. Immediately outside the water snowline, the midplane temperature is lower, due to lower dust opacity and thus more efficient cooling. Turbulent α is on the contrary, higher, providing more efficient radial transport of matter. It leads to lowering the gas surface density in this gap, which in turn increases α (see Eq. (5)), creating the positive feedback and further deepening the gap. One of the possible mechanisms to create the initial decrease in the gas surface density is dust back-reaction, which can affect the inward flow of gas at the snowline. This effect was investigated by Gárate *et al.* (2020) for different initial dust-to-gas ratios. The radial variation of α itself lead to the appearance of gas substructures (Tong, Alexander, and Rosotti 2024). The combined effect of lower temperature and density creates a pressure minimum, which dust tends to avoid.

The dead zone, where α -parameter values are lower than 10^{-3} , includes the ice-free inner disc and has an approximately two times larger radial span than the iceless region. The distribution of α -parameter is shown in the right column of Figure 1. Inside the primary water snowline, the values of α are the lowest due to high surface density of gas. The dead zone is not axisymmetric and reflects the spiral structures of the gas distribution, as it is sensitive to Σ_g (see Eq. (5)). The spiral arms of the dead zone span to 15 – 25 au at 160 kyr, to 10 – 18 au at 350 kyr and to 10 – 14 au at 490 kyr. The comparison with the temperature distribution in Figure 1 indicates that α and T_{mp} are anticorrelated, as higher viscosity provides faster accretion, hence lower surface densities and more efficient cooling. Similarly, a lot of dust accumulates in the dead zone, increasing opacity, which hampers cooling.

The icy dust ring at 1 – 2 au is especially interesting in the context of planet formation. In this ring, dust-to-gas ratio exceeds 0.1, and surface densities of both gas and dust are increased by more than an order of magnitude compared to the adjacent regions. Due to the ice mantles that protect dust from fragmentation, the dust size reaches several cm, close to the values behind the water snowline. When the ring is established, it is self-supporting, in a sense that without external perturbation (e.g. sharp change in accretion flow from the outer disc), it can be stable for a long time, over tens of kyr.

The presence of water ice inside the dead zone was investigated by Vallet *et al.* (2023). They showed that in the discs around lower-mass stars, the turbulent heating in the inner disc can be low enough to allow the existence of ices. In our modelling the cooling of the inner region is assisted by the inner dust ring. The freeze-out has a positive feedback on dust growth due to higher ν_{frag} , which helps dust grow larger and further accumulate toward the pressure maximum in the ring. So in our modelling ices coexist with a lot of grown dust in the dead zone. Such an icy inner region appears to be a promising place for the formation of the volatile rich planets.

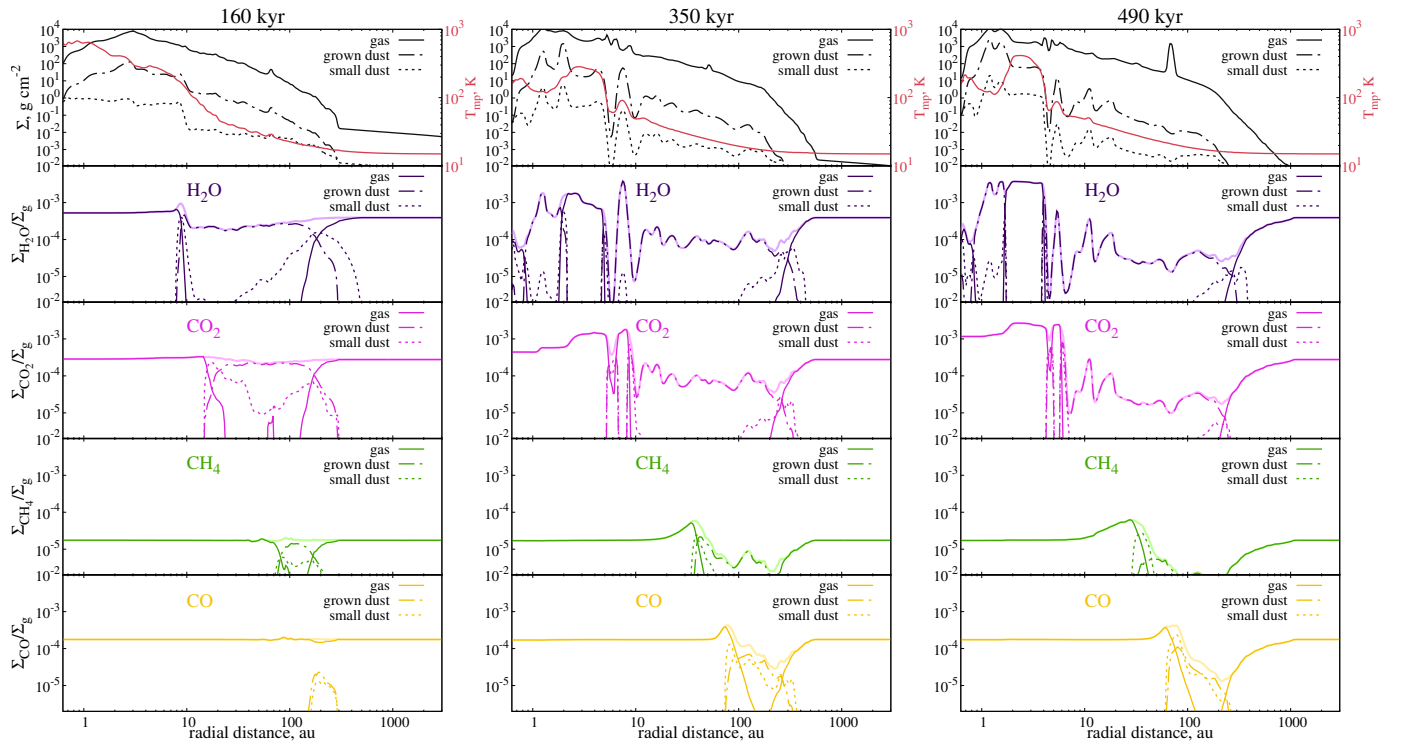


Figure 2. Radial distribution of azimuthally averaged surface densities of the volatiles in the gas and in the ice at various time instances in M1 ($M_{\text{core}} = 0.66 M_{\odot}$). Pale lines indicate the total surface density of species. The upper panels show surface densities of gas, small dust and grown dust, and the midplane temperature.

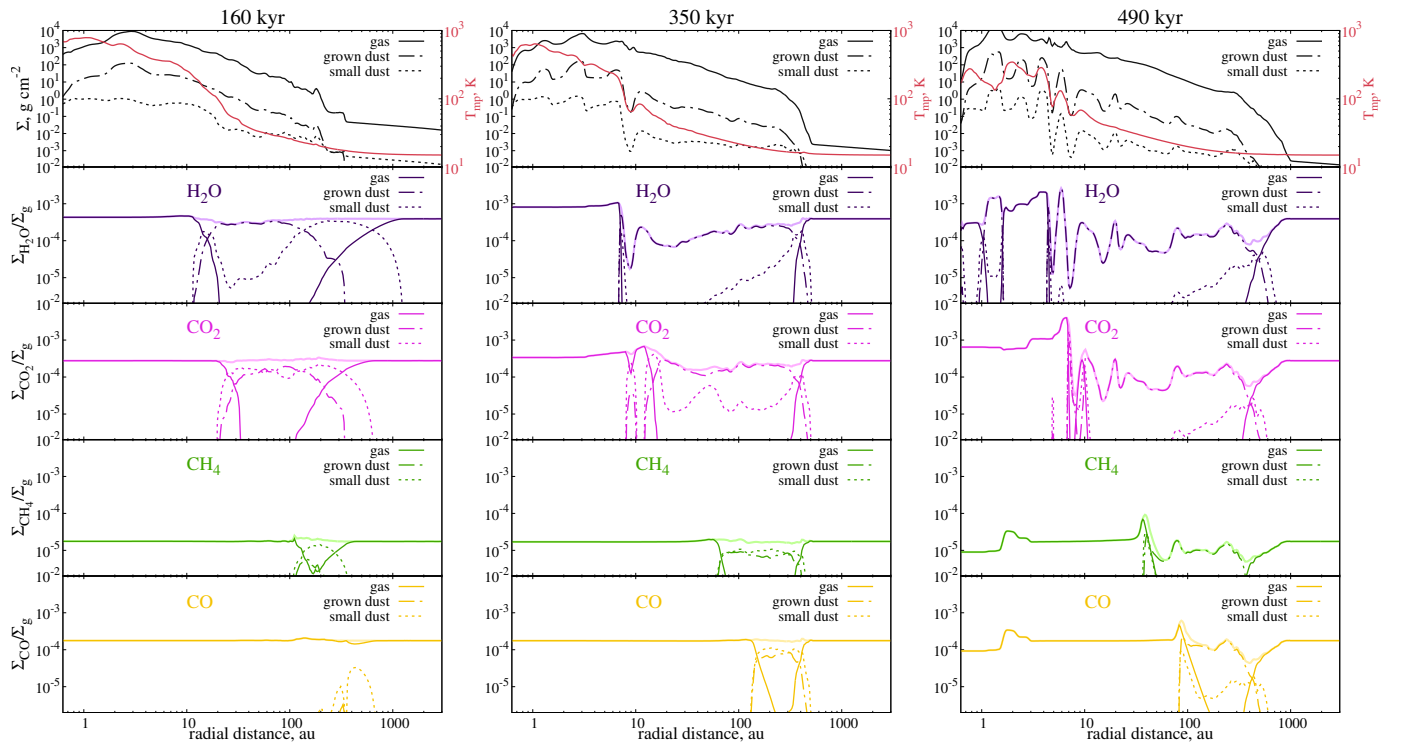


Figure 3. Same as Figure 2 but for model M2 ($M_{\text{core}} = 1 M_{\odot}$).

3.2 Distribution of volatiles

Even in the absence of chemical reactions, over the years of disc evolution the distribution of volatiles significantly changes compared to the initial one. This is the result of both phase transitions and dust growth and advection. Dust drift brings ices from the outer disc, enriching the inner disc with volatiles. Snowlines provide the conditions favouring accumulation of ices and gas-phase species. The formation of the established disc structures, such as dust and gas rings and spirals (see Section 3.1) leads to a complex pattern of intermittent snowlines. In this Section, we describe the main features of the molecular distributions and their implications for the composition of dust and gas at early stages of protoplanetary disc evolution.

Figures 2 and 3 show the azimuthally averaged radial profiles of the volatile species in models M1 and M2, respectively. As mentioned earlier, we define the snowline position as the location in the disc midplane where the amount of species in the gas equals to its amount in the ice (on both dust populations). This definition allows the snowline to have complex shape, characterised by different positions for each azimuthal direction. In the azimuthally averaged distributions shown in Figures 2 and 3, the position would only be approximate. The slope of the species distribution in the vicinity of the snowline reflects the degree of the axial asymmetry in the disc. Flatter distributions appear as the contributions sum up from the snowlines, the radial position of which vary at different azimuthal angles ϕ .

In our model setup, the volatiles can either have no snowline in the disc, or have two or more snowlines depending on the local conditions. Snowlines are absent for more volatile species (CO and CH₄) at earlier times or during bright luminosity outbursts, when the disc is too hot for them to freeze out. When there are two snowlines, the inner snowline in the disc is the one determined by thermal desorption. We refer to it as the primary snowline. The outer snowline is determined by photo-desorption, it lies in the embedding envelope outside of the body of the disc where optical depth is low. It must be noted that the gas-phase species outside this photo-snowline are vulnerable to photo-dissociation by the UV radiation. This process is not explicitly included in our chemical model, but can be assessed as in Molyarova *et al.* (2021).

More than two snowlines appear when the disc physical structure becomes more complex, mainly due to the presence of the ring-like structures. Species can freeze inside a cold dense dust ring, creating additional secondary snowlines, also governed by thermal desorption. The concepts of primary and secondary snowline is necessary for H₂O and CO₂, which have multiple snowlines at the later stages of disc evolution. For water, the inner icy region appears at ≈ 1 au at 490 kyr (see right column of Figure 3) inside a dense dust ring. For CO₂, the ring that appears at 7 au, outside the primary water snowline at 4 au, creates the inverted thermal structure in the region with T_{mp} close to the typical CO₂ sublimation temperature of 70–90 K. Increase in T_{mp} in these ring is caused by higher optical depth and consequently lower cooling on the viscously heated midplane.

Apart from the snowlines, the distributions of volatiles in Figures 2 and 3 present local radial variations in all of the species components, including total abundance of the species. The initial total abundance is kept only in the envelope. As the matter is being redistributed, abundances of all volatiles in the inner disc grow. Particularly, the process responsible for this is dust drift. It brings the grown ice-covered grains to the inner disc regions, where their ice mantles are sublimated and no longer move with the drifting silicate dust cores. The effect is stronger for less volatile species H₂O and CO₂: their abundance in the gas grows by a factor of a few inside their primary snowlines. For CO and CH₄ the effect is weaker, because there is less grown dust outside their snowlines, and those snowlines are not very much established at earlier times. Thus their abundances inside the snowline only grow by a factor of unity, except for the immediate vicinity of the snowline. Moreover, both CO and CH₄ have a bump in the gas-phase distribution just outside the dust ring at 1 au, that is absent in H₂O and CO₂. At the inner disc edge the abundances of CO and CH₄ in the gas are lower than the initial value.

The abundance enhancements appear most notably at the snowlines, with local bumps in all three phases at later times (after ≈ 350 kyr). They are produced by the combination of the dust radial drift and the azimuthal oscillations of dust and gas radial velocity, described in more detail in Molyarova *et al.* (2021) and Molyarova *et al.*, in prep. By 500 kyr, the surface density of gas-phase H₂O exceeds the initial value by a factor of 5, of CO₂ – by a factor of 7, of CH₄ – by 3.5 and of CO – by 2.5. Similar accumulation powered by turbulent diffusion was previously studied for CO molecule in axially symmetric model setup (Stammler *et al.* 2017; Krijt *et al.* 2018). Their results indicated similar enhancement in the gas phase by a factor of a few. In our non-axisymmetric approach, diffusion is not a necessary requirement, and the necessary transport is rather provided by azimuthal variations of radial velocity induced by disc self-gravity (Molyarova *et al.*, in prep).

Distributions of ices on small and grown dust are different as they are affected by dust growth and drift. In general, there is more grown dust than small by mass, and in most of the disc there is more ices on grown dust, particularly at later times. However, in the outer disc and at the earlier times, ices on small grains dominate. As initially all ices are on small dust, it seems inevitable that they will gradually move to the grown grains as small dust coagulates and turns into grown grains. However, near all the snowlines, amount of ices on small dust increases due to the effect of the spiral pattern. Ice abundances are determined by episodic sublimation and freeze-out in the warm spiral arms of the complex density and temperature pattern (see Section 3.3.2. in Molyarova *et al.* 2021). As adsorption preferably happens to the smaller grains due to their larger total surface area, there is much more ices on small dust in the wake of the spiral arms. This concerns the photo-desorption snowlines as well.

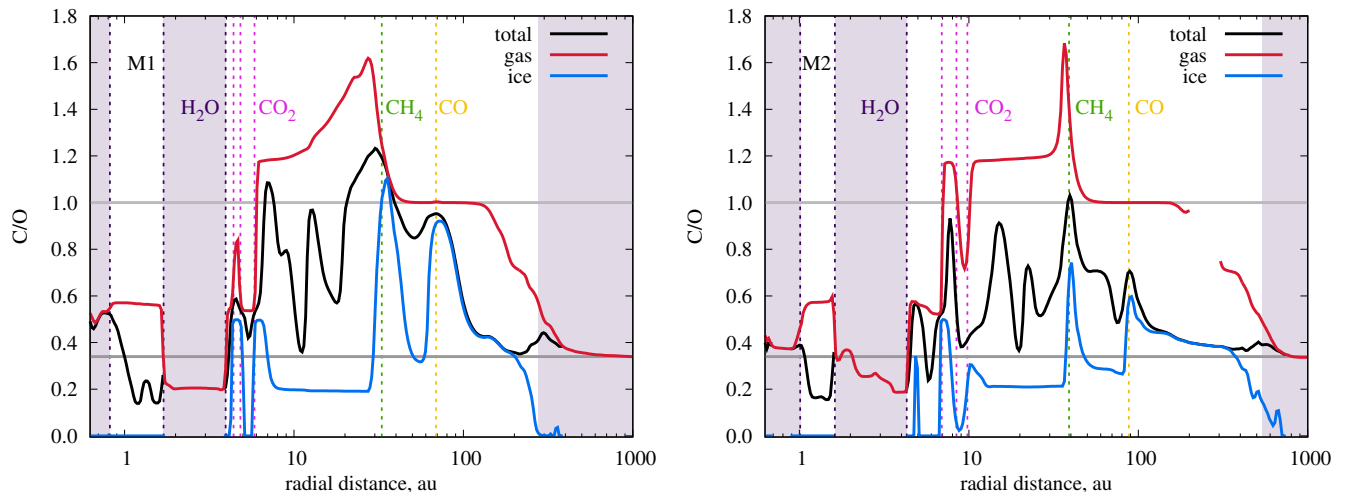


Figure 4. Radial profiles of the C/O ratio at 490 kyr in models M1 (left) and M2 (right). The plots show C/O in total (black), in the gas (red), and in the ice (blue). The C/O ratio in the ice (gas) is only shown for radial distances where the mass of the volatiles in the ice (gas) is larger than 0.1% of the total mass of the volatiles in the gas (ice). The grey horizontal line indicates the baseline C/O = 0.34. Positions of the snowlines are highlighted by vertical dashed lines. The regions where water (thus all other species) is in the gas are shaded with purple.

3.3 C/O ratios

Here we consider the relative amount of carbon and oxygen in the gas, on the surface of small and grown grains, and in total for all for all phases and disc locations. C/O ratio is seen as a perspective tracer of planet formation mechanisms (see Öberg, Murray-Clay, and Bergin 2011; Thiabaud et al. 2015). Therefore, we are especially interested in the regions of the disc and the volatile phase component where the C/O ratio declines from the total initial value (see below). Particularly, we are interested in C/O ratio noticeably above the initial value, as it was observed in atmospheres of exoplanets and suggests the formation of these planets in similarly carbon-enriched environments (Swain et al. 2009; Madhusudhan et al. 2011; Moses et al. 2013; Facchini et al. 2021).

The C/O ratio is calculated as the total number of carbon atoms contained in the molecules, divided by the total number of oxygen atoms in the molecules. This calculation can be done separately for the species contained in the gas phase, species on dust surface, or for the species in all phases. Thus, we calculate the C/O ratio in the gas, in the ice, and total C/O, respectively. For the ice species, we include both ices on grown and small dust grains. In some disc regions, the amount of carbon and oxygen in a particular phase is very low, e.g. in the ice phase inside the water snowline, where all the molecules are in the gas. For such cases, C/O ratio would not be representative of the chemical composition, so we exclude the corresponding computational cells from the consideration. We only display the C/O ratio if the mass of the volatiles in the phase is higher than 10^{-3} of the total mass of volatiles at a given location.

For the adopted molecular abundances based on Karin I. Öberg et al. (2011) and also used by Eistrup, Walsh, and van Dishoeck (2018), the baseline value is C/O = 0.34, which is in line with the gas-phase abundances in the ISM (≈ 0.36 , Przybilla, Nieva, and Butler 2008). This value is different from the typical solar value of ≈ 0.5 (Przybilla, Nieva, and Butler

2008), which is commonly used as a reference (e.g., Öberg, Murray-Clay, and Bergin 2011; Semenov et al. 2018). First, local galactic abundances changed since the Solar system formation 4.6 billion years ago (see, e.g., Appendix A in Bergin et al. 2024, for the comparison). Second, the difference also stems from inclusion or non-inclusion of the dust component. The stellar atmospheric abundances comprise all the elements present in the medium where the star formed, while the elements available for the volatiles are only a fraction of that. The values of the elemental abundances can be determined separately for the volatile (gas and ices) and the refractory (rocky dust grain cores) components of the ISM (Hensley and Draine 2021). Here, we do not take into account carbon and oxygen from the rocky cores of dust grains. Due to the model assumptions, the initial ice-to-rock mass ratio in our model is quite low (0.08 compared to 2–4 in Pontoppidan et al. 2014). Therefore, adding the elements from solid dust grains to those contained in ices would be misleading, as the former would dominate in the resulting C/O ratio. In this work, we concentrate on considering the C/O ratios of the volatile component (ice and gas), and compare them with the initial value of 0.34.

Figure 4 shows radial profiles of the C/O ratios averaged over the azimuthal angle ϕ by the end of the simulations, at 490 kyr. The key values of C/O ratio relevant in the context of planet formation are the initial value of 0.34, motivated by the comparison with the initial abundances, and 1.0, which is a boarder between carbon- and oxygen-dominated chemical regimes in the ISM and (exo)planetary atmospheres (see, e.g., Tielens 2005; Seager et al. 2005; Madhusudhan 2012).

By the age of 490 yr, the C/O ratio in both models is significantly different from the initial value. This concerns the total C/O ratio, as well as the C/O ratio in the gas and in the ice. Let us analyse the distributions of C/O ratios that we can see from Figure 4, moving inwards from the envelope to the centre. The main features of the C/O distributions are the

following:

- the C/O ratio in the envelope is close to the initial value 0.34 in the gas and in total, and it grows up to unity from the envelope to the CO snowline in the disc;
- around the CO snowline, the C/O approaches unity;
- between CO_2 and CH_4 snowlines the C/O in the gas is > 1 , and the C/O in the ice is below the initial;
- at the distances of tens of au, there are variations in the total C/O ratio that are not connected with any snowlines, or variations in gas- or ice-phase C/O ;
- ice-phase C/O ratios peak around all snowlines except water;
- inside the primary water snowline is the region rich in volatiles, with both gas- and ice-phase C/O are the lowest in the disc.

As expected, the key changes in the C/O ratio distribution are associated with the positions of the snowlines. There are two main processes. First, the freeze-out and desorption at the snowlines transfer the elements between phases, altering the C/O in the gas and in the ice. Second, the snowlines favour the accumulation of the respective volatiles both in the gas and in the ice, as was discussed in Section 3.2, pumping up the amount of both components and altering their proportion. Besides the snowlines, radial drift of grown grains (Weidenschilling 1977) transports the volatiles inwards. We discuss below which processes are responsible for the formation of the listed features.

C/O in the outer disc. In the surrounding envelope, outside the disc, all volatiles are in the gas due to photo-desorption, and C/O in the gas is close to the initial value of 0.34. Around the CO snowline and beyond, the C/O in the gas is close to unity, and in the gas C/O is higher than the initial, which requires explanation. The region beyond the CO snowline is usually described as the place where all species are frozen, thus having a stellar C/O ratio in the solid phase and practically no carbon or oxygen in the gas (e.g., Öberg, Murray-Clay, and Bergin 2011; Öberg and Wordsworth 2019; P. Mollière et al. 2020). In our simulations, only in model M2 there is a region where less than 10^{-3} of C and O is in the gas, and in model M1 such region is absent. Due to the asymmetric spiral structure that persists even at 490 kyr, even though most of CO is frozen beyond the snowline, there is a significant ($> 10^{-3}$) fraction of it in the gas. Additionally, the position of CO snowline itself is significantly affected by the dust drift, as it declines from the equilibrium between adsorption and desorption. The indistinctness of the CO snowline also helps CO to persist in the outer regions: all other species are ultimately frozen, so they are efficiently carried away to the inner disc via radial drift, while this works worse for only partially frozen CO. It creates relative overabundance of CO in the outer disc, elevating the total C/O ratio and later the ice-phase C/O ratio, when the preserved CO freezes out. Between the CO ice line and the envelope, there is a gradient of C/O in the gas due to photo-desorption of the ices. The last molecule to be photo-desorbed is water, which returns oxygen to the gas phase at the farthest radial distance.

C/O ≈ 1 around the CO snowline. Beyond the CH_4 snowline, CO dominates the composition of volatiles in the gas phase, leading to the gas-phase C/O close to unity, the value characteristic of the CO molecule. At the CO snowline, the CO dominates the ice-phase composition as well. While dust drift substantially lowered the abundances of CO_2 and H_2O by 490 kyr in these regions, CO ice accumulated at the snowline. This leads to the ice-phase C/O closer to 1, too, making the vicinity of the CO snowline a region where total amounts of C and O are similar.

High C/O in the gas, low C/O in the ice. In the disc regions beyond the primary CO_2 snowline, only CO and CH_4 are in the gas, meaning the dominance of carbon and $C/O > 1$. Consequently, the C/O in the ice is generally lower, around 0.2, as the ices are mainly H_2O and CO_2 rich in oxygen. This is consistent with the classical step-like picture of Öberg, Murray-Clay, and Bergin (2011), with the addition of carbon-rich methane allowing the $C/O > 1$. The midplane C/O ratios we simulate are difficult to directly compare with observations, which mostly trace the molecular layer above the disc midplane. High C/O ratios in the gas are indeed observed in many protoplanetary discs (e.g. Miotello et al. 2019), but they are considered to be a natural consequence of dust settling (Krijt et al. 2018; Krijt et al. 2020). Dust inward drift could also enhance this effect in the outer disc regions, creating the radial gradient of total C/O ratio in the disc. Observations of CS and SO emission coming from close to the midplane layers potentially indicate the presence of such radial gradient of the gas-phase C/O in the PDS 70 disc (Rampinelli et al. 2024).

Variations of total C/O. Throughout the disc, there are sharp changes in total C/O ratio not connected with any snowline. Most noticeable are the variations between CO_2 and CH_4 snowlines, where gas-phase and ice-phase C/O ratios are stable. These variations are associated with the disc substructures, particularly with the dense dust rings described in Section 3.1. The total C/O changes due to radial variations in dust-to-gas ratio: when it is higher, the total C/O is closer to the ice-phase C/O , and vice versa. Inside the dust-rich rings, H_2O and CO_2 ices are abundant, due to high surface density of dust relative to gas. At the same time, CO and CH_4 in the gas phase have similar surface densities inside dust rings and between them. Thus, in the dust rings, CO_2 and water are overabundant, leading to lower total C/O ratio. We consider this effect in more detail in Section 3.5. Variations of the total C/O ratio due to dust substructures are also present in the cold ring at ≈ 1 au.

C/O peaks at the snowlines. There are peaks of the C/O ratio in the ice right outside the snowlines of CO_2 , CH_4 and CO, produced by the accumulation of the respective ices (see Figures 2 and 3). In M2 model, the amount of CH_4 and CO ices at their respective snowlines becomes comparable with or even larger than those of CO_2 and H_2O (compare the right panels of Figure 3), leading to C/O in the ice $\approx 0.6 - 0.9$. In model M1, the accumulation is more prominent, so the C/O ratio in the ice approaches unity at CO snowline and > 1 at the methane snowline. These peaks distort the pattern of generally

low C/O ratio in the ice and preset additional regions where carbon-rich planetesimals could be formed, and carbon-rich pebbles could be accreted onto forming protoplanets. At the snowlines of H₂O and CO₂, the C/O in the ice approaches the C/O ratios of these molecules, 0 and 0.5, respectively.

Lower C/O inside the water snowline. Inside the primary water snowline, the C/O ratio is generally lower than outside of it, close to the initial 0.34. Contrary to the outer regions depleted of ices due to the radial drift, the disc parts inside and around the water snowline are enriched in volatiles, and particularly of oxygen-rich water and CO₂. Total and gas-phase C/O ratios vary from ≈ 0.2 to 0.6, as the secondary water snowlines add more substructure to the C/O distribution. The regions where the only ice is water and the ice-phase C/O = 0 are the inner cold dust ring at 1 au and the narrow annuli between water and CO₂ snowlines. The enrichment of the inner disc regions with oxygen as a result of dust radial drift is suggested by the resolved observations of molecules in protoplanetary discs (Banzatti et al. 2020).

These characteristic features of the C/O distributions are similar in the two presented models. The main difference is the radial distances where the borders between the zones are located; they are closer to the star in the less massive and thus colder model M1. This is mainly due to slightly different masses of the central star accumulated throughout 490 kyr of non-identical protostellar accretion history, which lead to different luminosity and thermal structure (see upper panels of Figure 5). Particularly, the stellar masses and luminosities at this time instance are: $1.07 L_{\odot}$ and $0.34 M_{\odot}$ (for M1), $1.89 L_{\odot}$ and $0.58 M_{\odot}$ (for M2). The less massive model M1 demonstrates overall higher C/O ratio in both phases.

3.4 Evolution of the snowlines and the C/O ratios

The positions of the snowlines are crucial for the values of C/O ratios, both because of the direct change through the phase transitions and the associated accumulation of volatiles. They depend on the local gas and dust properties, particularly on temperature. They can also be shifted inward due to dust drift (Piso et al. 2015). Snowlines evolve as the disc structure changes with time. In this Section, we consider the co-evolution of the snowlines and the C/O ratios and discuss the mechanisms of species redistribution over the disc.

The temporal evolution of the azimuthally averaged C/O ratios and the equilibrium positions of the snowlines is shown in Figure 5. It is evident from Figure 5 that the C/O ratio indeed follows the snowlines, particularly inside ≈ 10 au. The C/O structure changes throughout the disc evolution, and some key features only appear at later times.

One of the key factors affecting the disc thermal structure is the luminosity of the central source. In the upper panels of Figure 5, we show the evolution of total luminosity, which directly affects the positions of the snowlines. The luminosity is the sum of stellar and accretion components, coming from the protostar itself and gravitational potential energy of the accreted matter. The stellar luminosity gradually decreases as the protostar becomes more compact. Accretion luminosity

depends on the accretion rate, which is highly variable as a result of magnetorotational and gravitational instabilities in the disc (Kadam et al. 2019, 2020; Vorobyov, Khaibrakhmanov, et al. 2020). The simulated episodic luminosity outbursts are similar to those occurring in the observed YSOs (Connelley and Reipurth 2018), with their amplitudes of tens and hundreds L_{\odot} . In the more massive model M2, the outbursts are more frequent, brighter and occur until later times. The reasons behind this difference is the massive disc being more prone to both MRI and GI, which needs to be investigated in more detail in a separate study.

Snowlines of the least volatile of the considered species, H₂O and CO₂, exist in the model since the earliest phases of the disc formation. Even during bright luminosity outbursts ($\sim 100 L_{\odot}$) they do not disappear, but move farther away from the star. During the first ≈ 50 kyr the disc is spreading out, it is highly asymmetric and dynamic, so the snowline positions oscillate. Later on, the disc generally cools down, and the snowlines gradually move toward the star (except during the outbursts). In model M2, between 130 and 500 kyr, the primary water snowline moves from 12 to 4.5 au; the primary CO₂ snowline moves from 23 to 7 au. In model M1, the water snowline moves from 9 to 4 au, and the CO₂ snowline moves from 17 to 4.5 au.

Despite a factor of two different binding energies of H₂O and CO₂ (5770 and 2360 K, respectively), the locations of their primary snowlines do not differ much due to the steep radial temperature gradient around these distances (see upper panels of Figures 3 and 2). Inside 10 – 20 au, T_{mp} is determined by heating mechanisms other than external irradiation: viscous heating, gas work (PdV heating), heating by shocks and energy transport with advection. This also means that the water snowline is less sensitive to the level of irradiative heating, thus only slightly affected by the luminosity outbursts. The temperature change is particularly sharp at the water snowline(s), with the absolute value of the approximated power-law slope of 1.5 – 6. High surface density of dust in water-ice-free regions makes cooling less efficient and leads to locking up the produced heat and consequently higher temperatures. Besides, both these species have multiple snowlines due to the formation of ring-like substructures with the conditions close to the borderline between their frozen and gaseous state. These additional snowlines also affect the C/O distributions.

Methane and CO are the more volatile species in our model. They either have zero or two snowlines in the disc. The snowlines are absent during the outbursts brighter than $\approx 100 L_{\odot}$ for methane and $\approx 200 L_{\odot}$ for CO. Until approximately 200 – 250 kyr, there is no established CO snowline inside the disc. For example, at 160 kyr (see lower left panel in Figures 3 and 2) there is CO ice on both small and grown dust, but their amount is an order of magnitude lower than that of the gas. Additionally, most of this ice is located at the outer disc edge, where gas and dust surface densities sharply drop. Similar distribution appears for CO and CH₄ during bright outbursts: their ices are present in some disc regions, but due to non-axisymmetric disc structure, they do not dominate in the averaged profiles, and there is no common snowline for

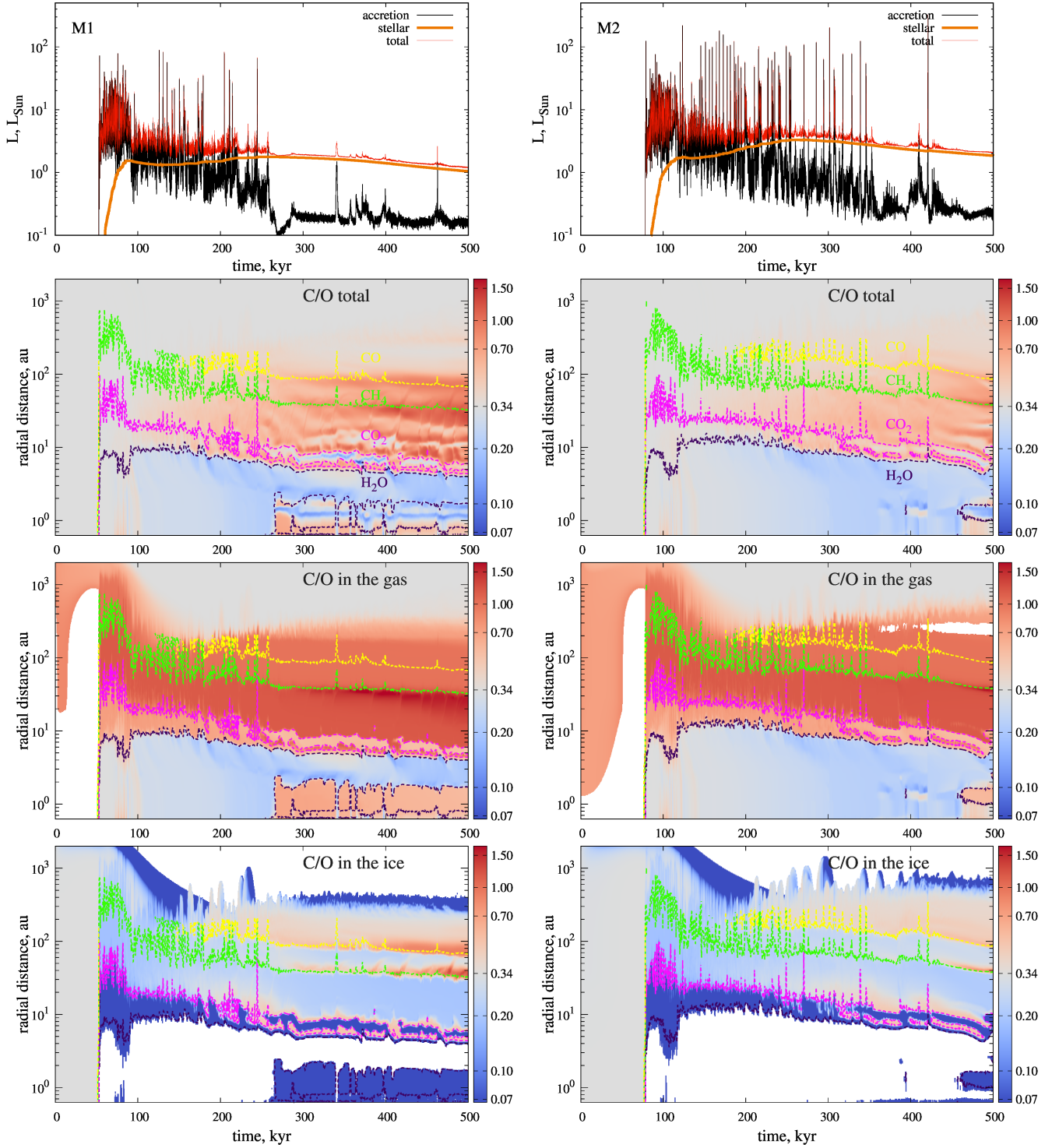


Figure 5. Evolution of central source luminosity and C/O ratio in models M1 ($M_{\text{core}} = 0.66M_{\odot}$, left) and M2 ($M_{\text{core}} = 1M_{\odot}$, right). The upper panels show stellar and accretion luminosity depending on time. Below are, successively, total C/O ratio, C/O in the gas, and C/O in the ice, depending on time. The C/O values above and below the initial value of 0.34 are coloured in shades of red and blue, respectively. The regions with low abundances of both carbon and oxygen, either in the gas or ice phases, are shown in white. Coloured contours correspond to the positions of the snowlines. Photo-dissociation snowlines are not shown.

the whole disc. There are no secondary snowlines of CO or CH₄, because there is no prominent gas and dust structures in the outer disc where these species are frozen.

Snowlines divide the disc into several zones with different characteristic C/O ratios. However, the chemical composition and C/O ratios in these zones change with time. One of the distinct zones is the region where water is not frozen, shaded with purple in Figure 4 and circumscribed by the dark purple dotted line in Figure 5. In this zone, all the species are in the gas phase, so the C/O ratio is initially close to 0.34. However, as the disc evolves, dust brings more volatiles from the outer disc. Particularly, the abundance of water grows most significantly, making C/O in the gas decrease with time. This happens because the main mechanism of the transport of the volatiles is dust radial drift, which works best in the regions where grown grains can sustain their mantles. Banzatti et al. (2020) suggest that dust growth and drift can be responsible for the observed anticorrelation between disc radius and H₂O emission, implying that the inner regions of small discs with are enriched in water brought by efficiently drifting grains. Water is the least volatile species in our model, it is frozen in the largest part of the disc, thus its distribution is most strongly affected by the dust drift. At later times, this zone is divided into two, when a cold dense dust ring forms at 1–2 au, which happens at ≈ 460 kyr in model M2 and at ≈ 270 kyr in model M1. Interior to the ring, water abundance in the gas is around an order of magnitude lower than outside of it in both models. This happens because the inward flow of gas-phase H₂O is “blocked” by the cold ring where it freezes and accumulates with the grown grains in the pressure maximum. So the C/O ratio in the gas at $r \lesssim 2$ au is determined by CO₂ and thus close to 0.5.

The C/O ratio in the ice is not defined in the envelope, where all ices are photo-desorbed, and in the warmest inner disc, where even water is in the gas. In disc regions where only water is frozen, the C/O ratio in the ice is zero. Before 200–250 kyr, when the disc cools down enough for CO to freeze out, the C/O ratio in the ice in the rest of the disc is close to 0.2. It is determined by CO₂ and H₂O ices, with a small contribution from the low-abundance CH₄. After that, when CO freezes out and CO snowline appears, the C/O ratio in the outer disc region becomes close to the initial value both in the ice and in total. This region beyond the CO snowline is frequently referred to in relation to giant exoplanets with stellar C/O ratios (e.g., P. Mollière et al. 2020; Öberg and Wordsworth 2019; Ohno and Ueda 2021). This region would be a perfect location for planets to accrete pebbles covered with icy mantles with the primordial elemental ratio, which would directly become part of the planetary atmosphere. However, pebbles are not initially present in the disc, and their existence in these outer regions is not guaranteed. Pebbles are dust grains large enough to move relative to gas e.g., Lambrechts and Johansen 2012; Lenz, Klahr, and Birnstiel 2019, and a fraction of the grown dust in our modelling can be classified as pebbles. The properties of pebbles and composition of their ice mantles in the same setting of the FEOSAD model were studied by Topchieva et al. (2024). They show that pebbles

appear in the disc as early as 50 kyr after its formation, and exist in a wide region of the disc. This partially includes the region beyond the CO snowline, but only the area of CO enhancement, where CO dominates in the ice composition and thus the C/O ratio in the ice is close to unity (see lower panels in their Figure 3).

As shown by Topchieva et al. (2024), ices on pebbles are dominated by H₂O and CO₂. In this case, relatively high values of the C/O in the ice (≈ 0.5) correspond to the regions where there is more CO₂, i.e. around the CO₂ snowlines. This is also the region where a prominent dust ring forms under the influence of the primary water snowline. It is characterised by accumulation of CO₂ and to lesser degree H₂O ice, as well as vapours, and relatively high amount of grown dust in the ring. The dust ring is situated between the two regions with C/O ≈ 0.34 in the ice. It presents another favourable location for accreting the ice content with close-to-initial C/O ratio.

The total C/O ratio in the disc also changed significantly from the initial value due to dust drift that redistributes the ices. The matter becomes more carbon-rich as the grains bring CO and CH₄ from the outer disc parts. This effect was previously investigated by Stammer et al. (2017) and Krijt et al. (2018) in their modelling of CO dynamics and dust evolution. However, as was shown by Krijt et al. (2018) and Krijt et al. (2020), vertical settling of grown grains towards the midplane is responsible for depleting the upper layers in the outer disc of gas-phase oxygen, which cannot be captured within our thin-disc modelling. The panels in the second row of Figure 5 demonstrate strong enhancement of total C/O ratio in the intermediate disc regions. In model M2, the total C/O ratio between 10–100 au becomes ≈ 0.7 after ~ 300 kyr, which is two times higher than the initial value. At the snowlines of CH₄ and CO₂ it approaches unity, mostly due to the accumulation of these species in the gas. In model M1, this process begins ≈ 200 kyr earlier and consequently leads to even higher total C/O ratio. At 400–500 kyr, most of the disc between 5 and 100 au has total C/O $\gtrsim 1$ in model M2, which demonstrates the powerful impact of dust drift.

A distinctive feature of the produced C/O distributions is the peaks of total and ice-phase C/O ratios around the CO and CH₄ snowlines. In model M2, the increase of the C/O ratios becomes noticeable only after ≈ 450 kyr, while in model M1 it starts to form around ≈ 300 kyr. Initial abundances of CH₄ and CO are lower than that of CO₂ and H₂O. As these species accumulate at their snowlines, the abundances become comparable, leading to C/O in the ice $\approx 0.6–0.8$ in model M2 and up to 1 in model M1. Similar accumulation is seen around CO₂ snowline, but unlike CO and CH₄ snowlines, it is also connected to the interaction with the dust ring structure and is considered in more detail in Section 3.5.

3.5 Two-dimensional structure

The disc is not axisymmetric even at later stages of its evolution (see Section 3.1 and Figure 1), which is also reflected in the distributions of volatiles and C/O ratios. Examples of 2D distributions of C/O in model M1 at two time instances are

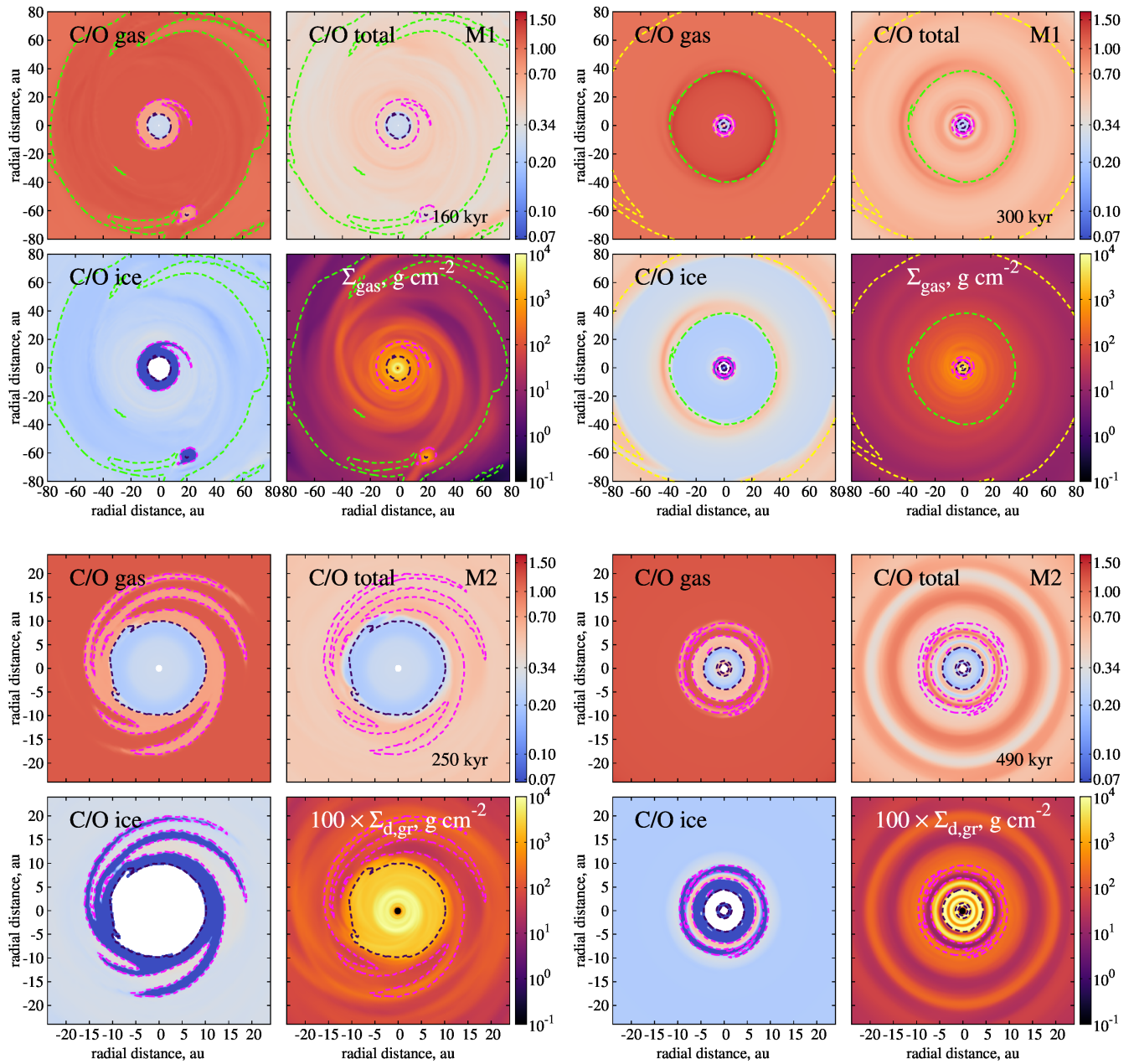


Figure 6. Distributions of C/O ratios and gas/dust surface densities. Model M1 160 kyr (upper left) and 300 kyr (upper right); model M2 250 kyr (lower left) and 490 kyr (lower right). Dotted lines mark the positions of the snowlines for H₂O (dark purple), CO₂ (magenta), CH₄ (green), and CO (yellow).

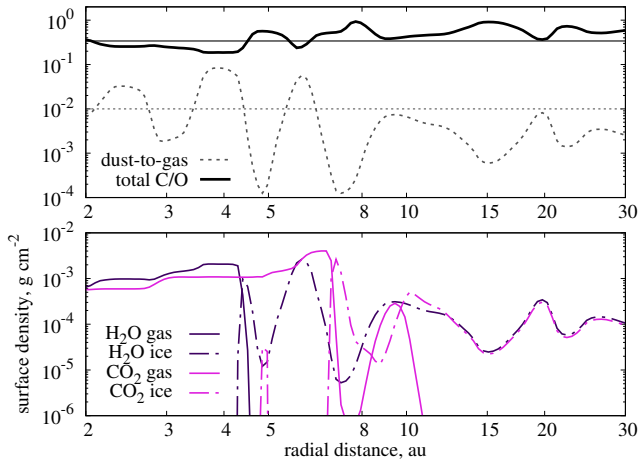


Figure 7. Averaged radial profiles of dust-to-gas ratio, the total C/O ratio, and CO₂ and H₂O in the gas and in the ice in model M2 at 490 kyr. The horizontal lines in the upper panel show the reference values for the C/O ratio (0.34) and dust-to-gas ratio (0.01).

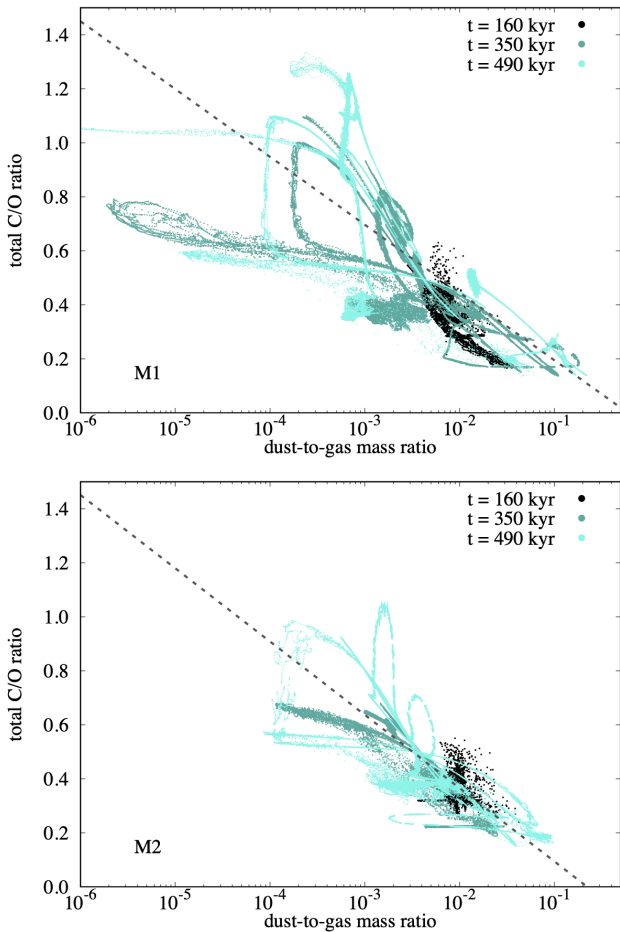


Figure 8. Dependence between total C/O ratio and dust-to-gas mass ratio in models M1 (upper panel) and M2 (lower panel). Three time instances are shown. The dashed line shows the fitted log-linear dependence for 490 kyr.

shown in upper panels of Figure 6. The left-hand side group of panels shows the structure that is characteristic of the earlier phases, the same time instance as the upper row in Figure 1. The prominent spiral structure and a clump both have their reflection in the C/O ratios. The snowlines of CO₂ and CH₄ have clearly non-regular shape affected by the spiral pattern of the gas, with blobs of frozen methane inside the main snowline. Inside the clump, the temperature is higher (see Figure 1), and both CO₂ and water are in the gas. The separation between gas-phase and ice-phase C/O ratios is clear, but the total C/O ratio in the clump is similar to the surroundings and is only slightly above the primordial value. The gas-phase C/O ratio inside the clump is around 0.7, lower than in the surrounding gas at the same radial distances. Similar decrease of C/O ratio indicated by lowered CS/CO ratio was observed in the disc around DR Tau (Huang et al. 2024). Lifetime of the clump (several orbital periods) is too short for significant differentiation between gas- and ice-phase composition to develop, mainly because of insufficient numerical resolution. Focused studies with higher resolution are needed to explore the C/O ratio in the clumps as precursor of giant planets formed via disc fragmentation.

The upper right-hand side group of panels in Figure 6 features a later stage of the disc evolution in model M1. By 300 kyr, the accretion rate and the average positions of the snowlines are stabilised (see Figure 5). The spiral structure in the gas is much weaker but still present at $r > 10$ au. The CO snowline is established at ≈ 80 au. The 2D shape of the snowlines is more circular at 300 kyr, particularly for the less volatile CO₂ and H₂O. The effect of spirals is still evident in the contours of the CO and CH₄ snowlines. At the outer side of these snowlines, at approximately 40 and 80 au, respectively, the C/O in the gas has local maxima, which are also seen in Figure 4. The one at 40 au also has a clearly spiral shape, repeating the pattern of the gas distribution. The radial span of these peaks is of the same scale as the dispersion of the respective snowline distance from the star. For example, at the CH₄ snowline the C/O peak is ≈ 10 au wide, and the snowline is at 28 to 37 au distances. Similar accumulation powered by diffusion of water vapour was shown, e.g., by Drązkowska and Alibert (2017). In addition to diffusion, in our modelling, the species are delivered outward from the snowline due to the dynamic shape of the snowline and two-dimensional movement of gas and dust (see Molyarova et al. 2021, and Molyarova et al., in prep).

In more massive model M2, the shape of the snowlines remains complex for longer times. Examples of C/O distributions in M2 are shown in the lower panels of Figure 6. The radial scale is chosen so that CO₂ and H₂O snowlines are seen in more detail. At 250 kyr, even the grown dust distribution still has spiral pattern, and CO₂ snowline is following its complex multi-armed shape. The accumulation of CO₂ at the snowline is also very efficient, but it does not strongly affect the C/O ratios, as it drives them to the value 0.5 of the CO₂ molecule, which is close to the intrinsic value. The complex-shaped region between these snowlines has the ice-phase C/O ≈ 0.7 . This pattern moves and changes its shape, thus affecting all

radial distances between 10 and 20 au. The total C/O ratio is slightly above the ambient value, approaching 0.5, because CO₂ in both phases begins to accumulate in this region.

At later times, the C/O distribution becomes more complex due to the presence of disc substructures, particularly the dust rings. The lower right-hand side group of panels in Figure 6 show this in more details. First, the temperature and density variations across the dust rings lead to the formation of multiple CO₂ and H₂O snowlines. An additional annulus of icy CO₂ appears in a relatively cold region between the dense dust rings at 6–7 and 8–13 au. The dust rings are warmer due to higher optical depth and active heating by disk internal sources, and the inner edge of the 6 au ring is warm enough to sustain gas-phase CO₂. Second, the accumulation of icy dust grains in the rings alters the total C/O ratio. The total C/O ratio anticorrelates with the distribution of grown dust grains: inside the dense rings it is close to the initial value of 0.34, while between the rings, it is higher and reaches 0.8–0.9. At the same time, neither ice-phase, nor gas-phase C/O ratio displays any noticeable variations at 12–25 au, but they do have variations at $r < 12$ au, following the dust ring pattern.

The total C/O ratio is defined by the combination of the ice- and the gas-phase component. Their relative contribution is proportional to the dust-to-gas mass ratio. This is illustrated in Figure 7. Within the rings, the total C/O is dominated by ices of oxygen-rich species CO₂ and H₂O, particularly on grown dust accumulated in the pressure maxima. For example, there is a lot of water ice at 6–7 au, and its contribution to the total C/O is weighted with high dust-to-gas ratio of almost 0.1, so the resulting total C/O is lower than the initial value. At the same time, at ≈ 5 au, dust-to-gas ratio is around 10^{-4} . The dominant species there are in the gas, ice surface densities are 1–2 orders of magnitude lower, so the total C/O ratio goes up. In the wide dust ring at 9–13 au, both H₂O and CO₂ contribute, although at the warmer inner edge of the dust ring CO₂ is sublimated. The value of total C/O is approaches 0.34, also elevated by the presence of gas-phase CO and CH₄. Beyond ≈ 10 au, both H₂O and CO₂ are frozen, and the variations of the total C/O ratio are clearly anticorrelated with the dust-to-gas ratio and the position of the rings. Between the dust rings, where contribution of ices is low, the C/O is determined by CO and CH₄ gases, and reaches values of ≈ 1 .

The anticorrelation between the total C/O ratio and dust-to-gas mass ratio is an interesting finding. It is illustrated in Figure 8 for both models. Only the points within the disc are shown, with $\Sigma_{\text{gas}} > 0.1 \text{ g cm}^{-2}$. The pattern obviously changes with time, but the anticorrelation persists. Model M1 demonstrates wider variety of C/O and dust-to-gas ratios. The disc points are grouped in tangled curved "branches", some of them steeper than others. The "width" (or spread) of these branches is determined by the azimuthal substructures. In the axially symmetric parts of the disc the values of dust-to-gas ratio and the total C/O are similar at a given radial distance. Different branches, which can be closer to vertical or horizontal orientation, are the result of the radial variations in the ice-phase C/O ratio and in ice fraction relative to the dust silicate cores. Horizontal branches correspond to weak or absent anticorrelation.

For example, near the snowlines of carbon-rich species, C/O in the ice is high and close to that of the gas, which decreases the effect of dust mass fraction on the total C/O. In areas with no ices, the anticorrelation is also irrelevant, because the total C/O is determined entirely by the gas phase. Vertical branches, on the contrary, correspond to the strongest anticorrelation effect, which is expected in the regions between the snowlines, where ice-phase C/O is the lowest. The identified anticorrelation in Figure 8 is similar to the results of chemical population synthesis modelling (Cridland *et al.* 2019, 2020) showing that the more solids a planet accreted in the disc, the lower the C/O ratio is in its atmosphere.

We fit the data for $t = 490$ kyr with a linear law (taking the logarithm of dust-to-gas ratio) and obtain the following fits: $C/O = -0.056 - 0.25 \log_{10}(\xi)$ for model M1, and $C/O = -0.18 - 0.27 \log_{10}(\xi)$ for model M2. Here, ξ is the dust-to-gas mass ratio. The correlation coefficients are -0.54 for M1 and -0.57 for M2. At the shown earlier times (160 and 350 kyr), the correlation coefficient changes between approximately -0.9 and -0.5 , which indicates noticeable anticorrelation throughout the disc evolution.

We note that these C/O ratios only include the volatile component, without the contribution from the refractory material. Although the refractory material is typically considered as silicates, which are rich oxygen, it contains a significant amount of carbon, with the resulting C/O ≈ 0.5 (see Table 2 in Hensley and Draine 2021). This solid carbon can be subject to carbon grain destruction (Lee, Bergin, and Nomura 2010; Gail and Tieloff 2017; Wei *et al.* 2019), but this process should be treated separately, as it also affects the gas-phase carbon abundance. Taking refractory cores into account should affect the dependence between total C/O ratio and dust-to-gas ratio, as adding more rock would make the C/O ratio closer to 0.5. Thus the degree of the anticorrelation must be affected by the composition of rocky cores, but the anticorrelation itself should remain even when refractories are included, because the C/O ≈ 0.5 is still lower than typical C/O of the gas in most of the disc ($\gtrsim 1$).

Dust rings are detected in the majority of the observed protoplanetary discs (Long *et al.* 2018; Huang, Andrews, Dullemond, *et al.* 2018). They are considered as a plausible sites of planet formation (Carrera, Johansen, and Davies 2015; Yang, Johansen, and Carrera 2017; Li and Youdin 2021; Lee, Fuentes, and Hopkins 2022; Jiang and Ormel 2023). The anticorrelation between the total C/O ratio of the volatiles and dust-to-gas mass ratio that we point out is a logical consequence of ices having typically lower C/O ratios and being attached to dust grains. If planets are formed in the dust rings with high dust-to-gas ratios ($> 10^{-2}$), either exclusively from solids, or with the inclusion of the dust component, this would imply that their material initially has lower C/O ratio of ≈ 0.5 and below. To reach higher C/O ratios up to unity and above, which are observed in many exoplanets, these planets would need to migrate and accrete carbon-rich gas from regions other than their immediate formation sites inside the dust rings. In case if planet formation occurs independently of the dust rings, e.g. in the GI, their material is not determined by this anticorrelation.

4. DISCUSSION

Our simulations present a wide range of C/O ratios in the disc in different phases evolving with time. For the atmospheres of giant exoplanets, a variety of C/O ratios were retrieved, too. Here we can compare them to identify the disc regions and times where the chemical and physical conditions for planet formation are consistent. Most of the exoplanets for which the atmospheric composition was retrieved have super-stellar C/O ratios (Hoch et al. 2023; Weiner Mansfield et al. 2024), which draws more attention to carbon-enriched areas. They are suggested to form by core accretion, and accreting mostly the gas, which is typically more carbon rich (beyond water snowline). A lot of planets are observed to have stellar or slightly super-stellar C/O (e.g., P. Mollière et al. 2020; Zhang et al. 2021; Smith et al. 2024; Sing et al. 2024; Nortmann et al. 2024, and many others). One way to form such planets is gravitational instability, which includes solids and gas together, thus undifferentiated matter is suitable for producing planets with stellar C/O. Disc fragmentation to clumps due to GI requires particular conditions (Meru and Bate 2010; Vorobyov 2013), and the direct collapse of gravitationally unstable clumps tends to produce rather massive objects (e.g. $\approx 5 M_J$ planets and $\approx 60 - 70 M_J$ brown dwarfs, see Figure 4 in Vorobyov, Zakhzhay, and Dunham 2013) at larger radial distances ($> 10 - 100$ au, see Vorobyov, Zakhzhay, and Dunham 2013; Kratter and Lodato 2016). GI can also assist the assemblage of planetary cores (Nayakshin 2010a, 2010b; Nayakshin, Helled, and Boley 2014; Vorobyov and Elbakyan 2019). A planet formed through core accretion can also accrete planetesimals, which can be covered with ice, and enrich the atmosphere with oxygen, making the C/O ratio close to the initial stellar value. There are particular exoplanets, where lower than stellar C/O ratio is observed in the atmosphere, such as β Pic b (GRAVITY Collaboration et al. 2020; Worthen et al. 2024), HD 209458 b (Xue et al. 2024), or HD 189733b (Fu et al. 2024). Such planets need even more enrichment in ices with low C/O, which makes the regions with low C/O in the ice also more attractive sites for planet formation.

Gravitational instability implies that the planet forms from a mix of gas and dust (Bodenheimer 1974), this is why it is suitable to explain the formation of planets with solar, or unaltered C/O ratios. In our modelling, GI would be associated with the total C/O ratio, which we find to be significantly variable, too. For GI to form a planet with a primordial C/O ratio, it has to occur during the first 100 kyr after the disc formation. At later times, the total C/O ratio changes, and the only region with the primordial C/O ratio is the very outer disc parts, at > 100 au, which is the part of a protoplanetary disc, where conditions for GI are the most consistent with the observed properties of these objects (Rafikov 2005). Planet formation through GI is indeed more likely at earlier evolutionary stages, when gas surface density is higher (Armitage 2010). We can highlight the areas where planet formation via GI is possible in our modelling as the regions where $Q_{\text{Toomre}} \leq 1$. They are shown in the upper panel of Figure 9 for model M1. These regions appear between $\approx 10 - 100$ au before ≈ 300 kyr.

However, at later times, clumps could appear in the disc as a result of an external perturbation, such as a stellar flyby (Thies et al. 2010). In this case, the planet would be formed from the material with altered C/O ratio, most probably with elevated amount of carbon, as the regions outside $5 - 10$ au are typically more gravitationally unstable. This means that GI can produce planets with super-solar C/O ratios, if it is induced by external influence at later stages of disc evolution.

Core accretion is another most widely discussed scenario of giant planet formation. Accretion of gas should produce atmospheres with the C/O ratio close to the one in the gas phase of protoplanetary disc. However, dust grains are also accreted, so pebble and planetesimal accretion can enrich the atmosphere in volatile components (Mordasini et al. 2016; Danti, Bitsch, and Mah 2023). This makes atmospheric C/O ratio closer to the ice-phase C/O, but in case of gas giants, the amount of the solids needed to compensate the prevalence of carbon in the gas should be quite high, up to hundreds of Earth masses (GRAVITY Collaboration et al. 2020). The C/O ratios in exoplanetary atmospheres are often interpreted in terms of pebble accretion, so planets with stellar C/O ratios are assumed to form in the environments where solid phase C/O is unprocessed and thus close to the initial value. One of such locations is beyond CO snowline, where most of the carbon- and oxygen- bearing material is in the ice, e.g. for Jupiter (e.g. Öberg and Wordsworth 2019; Ohno and Ueda 2021). In our models, this is rather the vicinity of the CO₂ snowlines, and the pebbles beyond the CO snowline are mostly covered with carbon-rich CO ice (Topchieva et al. 2024). Additionally, the CO snowline is typically very far from the star (> 40 au), so such scenarios must rely on planet migration to obtain their current location. Interpretations relying on chemical modelling extend this region to include the area beyond CO₂ snowline due to additional chemical processing of CO in this region, e.g. HR 8799e (P. Mollière et al. 2020). This puts milder constraints on the original distance from the star where pebbles should be accreted and requires less migration. Modelling of planet formation and migration including pebble and gas accretion puts the formation location of planets with super-solar C/O ratios beyond water and CO₂ snowlines (Bitsch, Schneider, and Kreidberg 2022).

In our modelling, the C/O in the ice is close to initial value in the regions beyond CO snowline, excluding the area of CO accumulation. Between CO and CO₂ snowlines, it is lower, as our model does not include chemical processes apart from adsorption and desorption. However, there is another region with C/O in the ice close to initial. The vicinity of primary water snowline and the ring induced outside of it has values of C/O in the ice only slightly above the initial value of 0.34. It is surrounded by the snowlines of CO₂. This region could be another favourable location for forming planets with the stellar C/O. As it is situated closer to the star, it would imply less migration.

Rare planets with lower than stellar C/O ratio, such as β Pic b (GRAVITY Collaboration et al. 2020; Reggiani et al. 2024), HD 209458 b (Xue et al. 2024), HD 189733b (Fu et al. 2024), or KELT-1 b, Kepler-13A b and WASP-79 b

(less precisely determined, see Hoch *et al.* 2023), need to have accreted a lot of oxygen-rich ice. Therefore, they are more likely to accrete solid material in the regions with the lowest ice-phase C/O ratios. The most suitable region would be at the distances between H₂O and CO₂ snowlines, where ice mantles are made of pure water. However, in our modelling results, this region is very small, typically only a few au wide, as the snowlines are close to each other. This is because of steep temperature profile in this region, which is a result of the significant contribution of non-irradiation heating mechanisms, particularly viscous heating. Beyond CO₂ snowline, there are also regions with relatively low (0.2–0.3) C/O in the ice, but much more solids need to be accreted in such areas to compensate for the excess of carbon from the gas.

Let us summarise the above constraints on planet formation locations and mechanisms implied by our simulated C/O ratios. Core accretion is suitable for forming planets with high C/O (≈ 1) in the atmosphere around the snowlines of CO, CH₄ and CO₂, or anywhere beyond CO₂ snowline if they did not accrete much solids. Planets with stellar or slightly super-stellar C/O ratio need to accrete (a lot of) oxygen-rich solids to compensate their initially high C/O inherited from the gas. The locations where this is possible is between CO₂ and CH₄ and between CO and CH₄ snowlines. Planets with low C/O ratio could accrete ices between H₂O and CO₂ snowlines. Snowlines are favourable planetesimal formation sites, so the planets that accreted planetesimals/pebbles there can have altered C/O ratios. The values will be lower than the initial if they form at the water snowline, and higher if they form at the snowlines of carbon-rich species. At the same time, to obtain planets with stellar C/O formed at the snowlines, these planets would need to migrate and accrete matter in different regions of the disc to make their C/O ratio close to the initial stellar value. Alternatively, planets with stellar C/O ratio can form via disc fragmentation through GI at earlier stages. Dedicated modelling of planet formation accounting for evolution of dust and volatiles is necessary to put more particular constraints on planet formation scenarios.

Planetesimals play an important role in delivering the ice-phase elements to planetary atmospheres. To form planetesimals, additional physical process is needed, such as streaming instability (SI, see Youdin and Goodman 2005), which is not explicitly included in our modelling because of insufficient numerical resolution and simplified vertical disc structure. However, we can post-process the simulation results to check if the conditions for SI are fulfilled in some regions of the disc where dust-to-gas ratio and dust size are enhanced, following Vorobyov *et al.* (2024). Dense dust rings forming at later stages (see Section 3.1) seem to be an ideal location for triggering the SI, which would ultimately lead to formation of planetesimals and then planets in the disc. Triggering the SI requires specific relations between local dust-to-gas ratio and Stokes number (Yang, Johansen, and Carrera 2017). The criteria vary depending on the model, we adopt them from Li and Youdin (2021). Another criteria would be the requirement of volume density of dust to exceed that of gas in the midplane (Youdin and Goodman 2005). We do not apply it, as in our modelling,

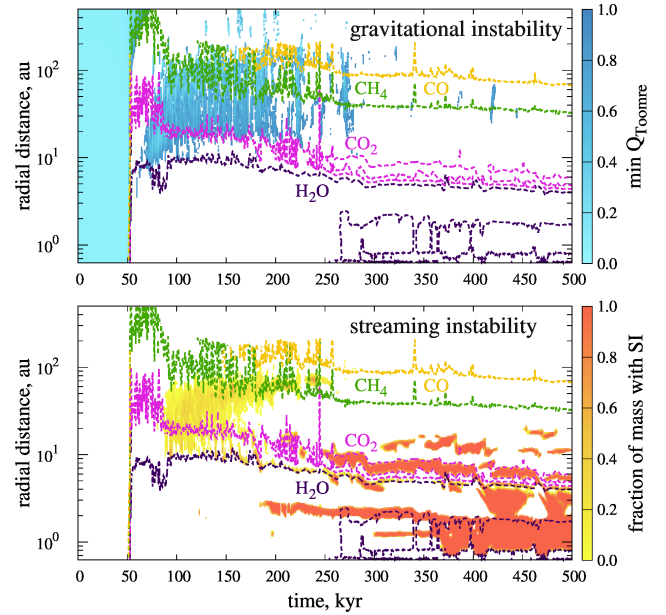


Figure 9. The disc regions where the conditions for GI and SI are fulfilled in model M1. The regions and times where there is no instability are shaded in white. In the upper panel, the colour indicates the minimum value of Q_{Toomre} at a given radius, if $Q_{\text{Toomre}} \leq 1$. In the lower panel, the colour indicates the fraction of mass at a given radius where SI can be triggered according to Li and Youdin (2021) criterion. Positions of the snowlines are shown for reference in dashed lines.

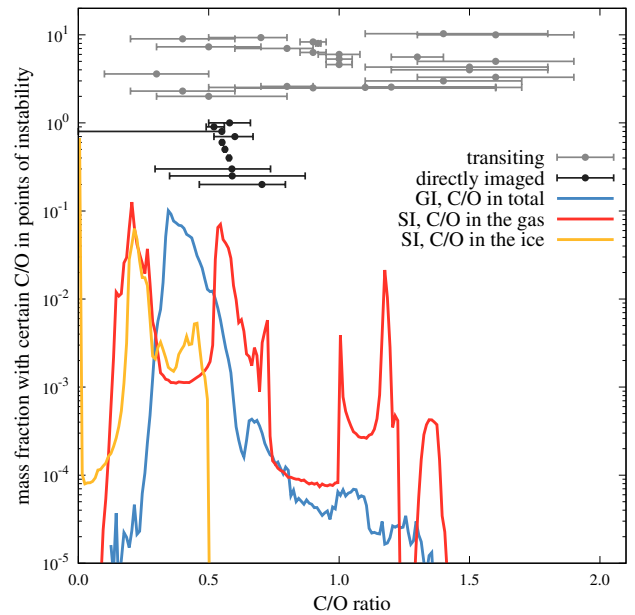


Figure 10. Distribution of C/O ratios in the regions where gravitational and streaming instabilities are triggered. For GI, total C/O ratio is shown, for SI, the C/O ratios in the ice and in the gas. Black and grey points show the observed C/O ratios in two populations of exoplanets, the data is adopted from Hoch *et al.* (2023).

the residual value of α is 10^{-3} which makes this condition unreachably outside of the dead zone. The regions in model M1 where the conditions of Li and Youdin (2021) are satisfied are shown in the lower panel of Figure 9. Most of the suitable regions are in the inner disc ($r < 20$ au) inside the dust rings, and appear after 200 kyr. However, there are some suitable regions between 10 – 100 au at earlier times, where SI could be triggered in the spirals.

The regions where GI and SI are possible shown in Figure 9 are separated in space and time, and they have different characteristic C/O ratios. We can sum up all the volatiles in these regions (throughout the disc lifetime) to assess typical C/O ratios of the planet-forming material. For GI, we exclude the pre-disc phase ($t < 53$ kyr) and consider the total C/O ratio, assuming both gas and solids are included in the forming planet. For SI, we separate the gas- and ice-phase C/O ratios. The formed planetesimals would only include the ices, however, if they form the planetary cores, these cores would also accrete gas. We note that the composition of the rocks, which are typically carbon-rich, is not included in our assessment. The resulting distributions of the C/O ratios in planet-forming regions are shown in Figure 10. For GI regions, the C/O distribution has a distinct and relatively narrow peak around 0.5. It is slightly higher than the initial value of 0.34. For SI regions, the ice-phase C/O is below 0.5, with major peaks at 0 and ≈ 0.2 , and the gas-phase C/O has a broad distribution with multiple peaks between ≈ 0.2 –1.4. Distributions of C/O ratios in the regions where GI and SI can be triggered are noticeably different.

It was shown by Hoch et al. (2023) that there are two different populations of C/O ratios observed in giant exoplanets. They find that directly imaged exoplanets have C/O ≈ 0.5 –0.8, while transiting hot Jupiters have a wider variety of C/O ratios (≈ 0.3 –1.7, see Figures 12 and 13 in Hoch et al. 2023), and suggest that these two populations could have different formation pathways. We add the C/O data of exoplanetary atmospheres compiled in Table 3 of Hoch et al. (2023) to Figure 10 (with arbitrary position at the y -axis). The narrow distribution of C/O ratios in the regions with GI is in step with the distribution of directly imaged exoplanets, albeit with a slightly shifted value due to our assumed initial conditions, while the wide range of C/O values in the regions of SI matches the variety of C/O ratios in transiting exoplanets. This could suggest that directly imaged exoplanets could form as a result of gravitational instability, which is also in line with their typically higher masses and orbital separations. At the same time, the transiting hot Jupiters could have experienced a lot of migration (Lin, Bodenheimer, and Richardson 1996; Dawson and Johnson 2018), during which they accrete material with a variety of C/O ratios both from the gas and solid phase. It suggests that they could also form in the core accretion scenario. The origin of wide separation planets was also investigated by Bergin et al. (2024), based on the comparison with the observed C/O > 1 in protoplanetary discs (including the full composition of solids). They conclude that both core accretion and gravitational instability can work as the formation mechanism of these planets.

Apart from (exo)planets, the C/O ratios can be measured

for the comets, which present the best preserved sample of the primordial composition of the ices in the Solar System. Spectroscopic measurements of molecular composition in the comae suggest that the C/O ratio of cometary ice is quite low, typically below 0.1 due to the dominance of water ice (A’Hearn et al. 2012; Seligman et al. 2022; Harrington Pinto et al. 2022). Although most comets are carbon-depleted, there are individual measurements of C/O in comets above 0.5, for example in C/2006 W3 Christensen and 29P/Schwassmann-Wachmann (Ootsubo et al. 2012; Seligman et al. 2022), or even close to 1 in C/2016 R2 (PanSTARRS) (Wierczos and Womack 2018; McKay et al. 2019). Additionally, high value of C/O ≈ 1 was observed in the interstellar object 2I/Borisov (Bodewits et al. 2020). Our modelling results show the ice-phase C/O = 0 in the vicinity of the water snowline, as well as low values between the CO₂ and CH₄ snowlines (≈ 0.2) and between the CH₄ and CO snowlines (≈ 0.3). These are the locations where comets could originate from. However, in the vicinity of the CO₂, CH₄ and CO ice lines themselves, the C/O ratio in the ice phase is much higher. The fact that carbon-rich cometary ices are extremely rare in the Solar System may indicate that planetesimals formed on ice lines from carbon-rich volatiles do not persist throughout the evolution of a planetary system. This means that they are likely to be included in larger bodies, which favours the snowline-aided planet formation scenarios (Drażkowska and Alibert 2017; Hyodo et al. 2021). This is also consistent with the abundance of exoplanets with high C/O (Weiner Mansfield et al. 2024), which could be formed around the snowlines of carbon-rich species. In the giant planets of the Solar System, the C/O ratios are not well constrained (Mousis, Cavalié, et al. 2024). However, the existing data suggest rather super-solar values for all giant planets except for Neptune (Cavalié et al. 2024); for Jupiter, the C/O ratio is assessed as ≈ 0.9 (Wong et al. 2004; Li et al. 2024).

Our model only considers four most abundant chemical species. However, there can be other more complex molecules in protoplanetary discs, which could affect the balance of carbon and oxygen. The most obvious candidate is methanol CH₃OH, which has the abundance similar to methane in the protostellar cores (Karin I. Öberg et al. 2011). It was also observed in a protoplanetary disc around an erupting star V883 Ori (Lee et al. 2019). We do not consider it in the model as its binding energy is close to that of water, thus the snowlines would have similar positions, but the abundance is an order of magnitude lower. However, it could somewhat increase the local C/O ratio in the inner regions where there are no other carbon-bearing species, such as the ice in the ring at 1 au. Including methanol would alter the distribution of the C/O ratio. Interactions between the ices considered in the model could also affect the results. As was recently shown by Ligterink, Kipfer, and Gavino (2024), trapping of volatile species inside the mantles of less volatile ices could have a significant impact on the distribution of C/O ratios.

Another important process missing in our modelling is gas-phase and surface chemical reactions. They could significantly affect the distribution of C/O ratio in the gas and in

the ice, particularly with high level of cosmic ray ionisation (Eistrup, Walsh, and van Dishoeck 2016) or if carbon grain destruction is considered (Cridland, Eistrup, and van Dishoeck 2019). One particular mechanism is the transformation of CO to CO₂ on the surface of dust grains, which can lead to the depletion of CO from both gas and ice phases between CO and CO₂ snowlines (Molyarova *et al.* 2017; Bosman, Tielens, and van Dishoeck 2018). Considering this mechanism can change the conclusions about planet formation location (P. Mollière *et al.* 2020). Nevertheless, radial variations of the C/O ratio are necessary to explain molecular emission of discs with gaps (Leemker *et al.* 2024), and they can only be result of dust dynamics. In order to more consistently describe the distribution of molecules and elements in the disc, the models combining dust evolution and dynamics with more complex chemistry treatment are necessary.

Our simulations adopt the thin-disc approximation and focus on the midplane of the protoplanetary discs, in order to capture the essential physics of self-gravity, thermal balance, and dust evolution in a global modelling within reasonable computational times. This means that some relevant processes connected with the vertical structure are inevitably excluded. For example, vertical mixing and dust settling affect the C/O ratio in the upper layers of the disc (Krijt *et al.* 2018; Krijt *et al.* 2020). Dust settling is implicitly included in our modelling through separate scale heights of down dust and gas (as well as small dust), affecting dust number density in the midplane. However, this approach does not allow to reproduce vertical stratification in dust properties and chemical composition, which is particularly relevant for the interpretation of molecular observations. Vertical structure is also relevant for the accretion of matter on forming giant planets, which should proceed in 3D manner through meridional flows (Morbidelli *et al.* 2014). Cridland, Bosman, and van Dishoeck (2020) showed that the C/O ratio in the atmospheres of giant planets is rather affected by the composition of the molecular layer than that of the midplane.

5. Conclusions

In this work, we studied the distribution of volatiles in a viscous self-gravitating protoplanetary disc with dust evolution using a thin-disc hydrodynamic code FEOSAD (Vorobyov *et al.* 2018; Molyarova *et al.* 2021). We calculated the C/O elemental ratio in the gas, in the ice, and in total, identified the key properties of the distribution of elements over 500 kyr of disc evolution and considered their implications for planet formation theory. Our main findings can be summarised as follows.

- The simulated C/O ratios in the regions where GI and SI conditions are fulfilled are consistent with the C/O ratios in two populations of exoplanets possibly formed in different mechanisms pointed out by Hoch *et al.* (2023). We show that narrow C/O distribution of directly imaged planets is consistent with their formation via gravitational instability, while a variety of C/O in transiting hot Jupiters is in line with their migration through varying C/O conditions after the formation via either core accretion or GI.

- The lower C/O ratio in the ice between the CO₂, CH₄ and CO snowlines is consistent with the typical composition of Solar System comets, while the higher value of C/O \approx 0.5–1 at these snowlines corresponds to the composition of rare carbon-rich comets. This may indicate that matter from the snowlines is hardly preserved during the evolution of the disc and planetary system, possibly due to the inclusion in to planets.
- The distribution of volatiles is affected by the disc substructures, such as rings and spirals, as well as by dust radial drift. Variations of physical conditions create multiple snowlines of CO₂ and H₂O inside 10 au. Dust drift of icy grains brings the volatiles from the outer to the inner disc, enriching the inner disc with both C and O. It also creates a radial gradient of the total C/O ratio: its value is around 0.2 where water is not frozen, and 0.6–0.9 where it is icy, compared to the initial value of 0.34.
- Volatiles accumulate at their snowlines in both ice and gas phases due to the combined effect of dust drift and azimuthal variations of gas and dust radial velocities in a self-gravitating, non-axisymmetric disc. The species with low initial abundances, such as CH₄ (or methanol not considered here), can significantly affect C/O ratio, as their accumulation at the snowline creates a bump in C/O in all phases above 1.0. The total mass of the model affects the timescales and the magnitude of the accumulation by a factor of two.
- Forming planets can accrete gas with C/O > 1 beyond CO₂ snowline, ices with C/O \approx 0.5–1 at the CO, CH₄ and CO₂ snowlines, ices with C/O \approx 0.2–0.3 between these snowlines and ices with C/O = 0 between H₂O and CO₂ snowlines. Planets with stellar C/O would need to migrate through these regions to acquire necessary composition or form via GI at earlier stages from the mixture of gas and dust with unaltered C/O ratio.
- Dust-to-gas mass ratio and the total C/O ratio are systematically anticorrelated, because in dust-rich regions the volatile composition is close to that of the ice (which is lower), and in dust-poor regions, gas determines the C/O ratio.

The connection between protoplanetary disc components and exoplanets based on their composition should be more thoroughly investigated in the models focused on the planet formation process. We emphasise that these models should also take into account the effect of dust evolution and dynamics on the distribution of the elements in the planet-forming material. Inclusion of chemical processes and more accurate consideration of the bulk composition of dust grains could also affect the C/O ratios of the planet-forming environment.

Acknowledgement

We are thankful to the anonymous referee for useful comments that helped to improve the manuscript. The computational results presented have been achieved using the Vienna Scientific Cluster (VSC) and the local computing facility of the Southern Federal University.

Funding Statement The work is supported by Russian Science Foundation grant 22-72-10029, <https://rscf.ru/project/22-72-10029/>

Competing Interests None

Data Availability Statement The data underlying this article will be shared on reasonable request to the corresponding author.

References

- A'Hearn, Michael F., Lori M. Feaga, H. Uwe Keller, Hideyo Kawakita, Donald L. Hampton, Jochen Kissel, Kenneth P. Klaasen, et al. 2012. Cometary Volatiles and the Origin of Comets. *ApJ* 758, no. 1 (October): 29. <https://doi.org/10.1088/0004-637X/758/1/29>.
- Aikawa, Yuri, Shoken M. Miyama, Takenori Nakano, and Toyoharu Umebayashi. 1996. Evolution of Molecular Abundance in Gaseous Disks around Young Stars: Depletion of CO Molecules. *ApJ* 467 (August): 684. <https://doi.org/10.1086/177644>.
- Akimkin, Vitaly, Eduard Vorobyov, Yaroslav Pavlyuchenkov, and Olga Stoyanovskaya. 2020. Gravitoviscous protoplanetary discs with a dust component - IV. Disc outer edges, spectral indices, and opacity gaps. *MNRAS* 499, no. 4 (December): 5578–5597. <https://doi.org/10.1093/mnras/staa3134>. arXiv: 2010.06566 [astro-ph.EP].
- Armitage, Philip J. 2010. *Astrophysics of Planet Formation*.
- Armitage, Philip J., Mario Livio, and J. E. Pringle. 2001. Episodic accretion in magnetically layered protoplanetary discs. *MNRAS* 324, no. 3 (June): 705–711. <https://doi.org/10.1046/j.1365-8711.2001.04356.x>. arXiv: astro-ph/0101253 [astro-ph].
- Audard, M., P. Ábrahám, M. M. Dunham, J. D. Green, N. Grosso, K. Hamaguchi, J. H. Kastner, et al. 2014. Episodic Accretion in Young Stars. In *Protostars and planets vi*, edited by Henrik Beuther, Ralf S. Klessen, Cornelis P. Dullemond, and Thomas Henning, 387–410. January. https://doi.org/10.2458/azu_uapress_9780816531240-ch017. arXiv: 1401.3368 [astro-ph.SR].
- Bai, Xue-Ning, and James M. Stone. 2013. Wind-driven Accretion in Protoplanetary Disks. I. Suppression of the Magnetorotational Instability and Launching of the Magnetocentrifugal Wind. *ApJ* 769, no. 1 (May): 76. <https://doi.org/10.1088/0004-637X/769/1/76>. arXiv: 1301.0318 [astro-ph.EP].
- Banzatti, Andrea, Ilaria Pascucci, Arthur D. Bosman, Paola Pinilla, Colette Salyk, Gregory J. Herczeg, Klaus M. Pontoppidan, et al. 2020. Hints for Icy Pebble Migration Feeding an Oxygen-rich Chemistry in the Inner Planet-forming Region of Disks. *ApJ* 903, no. 2 (November): 124. <https://doi.org/10.3847/1538-4357/abbc1a>. arXiv: 2009.13525 [astro-ph.EP].
- Benneke, Björn, Heather A. Knutson, Joshua Lothringer, Ian J. M. Crossfield, Julianne I. Moses, Caroline Morley, Laura Kreidberg, et al. 2019. A sub-Neptune exoplanet with a low-metallicity methane-depleted atmosphere and Mie-scattering clouds. *Nature Astronomy* 3 (July): 813–821. <https://doi.org/10.1038/s41550-019-0800-5>. arXiv: 1907.00449 [astro-ph.EP].
- Bergin, Edwin A., Richard A. Booth, Maria Jose Colmenares, and John D. Ilee. 2024. C/O Ratios and the formation of wide separation exoplanets. *arXiv e-prints* (June): arXiv:2406.12037. <https://doi.org/10.48550/arXiv.2406.12037>. arXiv: 2406.12037 [astro-ph.EP].
- Bergin, Edwin A., Fujun Du, L. Ilesedore Cleaves, G. A. Blake, K. Schwarz, R. Visser, and K. Zhang. 2016. Hydrocarbon Emission Rings in Protoplanetary Disks Induced by Dust Evolution. *ApJ* 831, no. 1 (November): 101. <https://doi.org/10.3847/0004-637X/831/1/101>. arXiv: 1609.06337 [astro-ph.EP].
- Binney, James, and Scott Tremaine. 1987. *Galactic dynamics*.
- Birnstiel, Tilman. 2023. Dust growth and evolution in protoplanetary disks. *arXiv e-prints* (December): arXiv:2312.13287. <https://doi.org/10.48550/arXiv.2312.13287>. arXiv: 2312.13287 [astro-ph.EP].
- Bisschop, S. E., H. J. Fraser, K. I. Öberg, E. F. van Dishoeck, and S. Schlemmer. 2006. Desorption rates and sticking coefficients for CO and N₂ interstellar ices. *A&A* 449, no. 3 (April): 1297–1309. <https://doi.org/10.1051/0004-6361/20054051>. arXiv: astro-ph/0601082 [astro-ph].
- Bitsch, Bertram, Aaron David Schneider, and Laura Kreidberg. 2022. How drifting and evaporating pebbles shape giant planets. III. The formation of WASP-77A b and τ Boötis b. *A&A* 665 (September): A138. <https://doi.org/10.1051/0004-6361/202243345>. arXiv: 2207.06077 [astro-ph.EP].
- Bodenheimer, P. 1974. Calculations of the Early Evolution of Jupiter. *Icarus* 23, no. 3 (November): 319–325. [https://doi.org/10.1016/0019-1035\(74\)90050-5](https://doi.org/10.1016/0019-1035(74)90050-5).
- Bodewits, D., J. W. Noonan, P. D. Feldman, M. T. Bannister, D. Farnocchia, W. M. Harris, J. -Y. Li, K. E. Mandt, J. Wm. Parker, and Z. -X. Xing. 2020. The carbon monoxide-rich interstellar comet 2I/Borisov. *Nature Astronomy* 4 (April): 867–871. <https://doi.org/10.1038/s41550-020-1095-2>. arXiv: 2004.08972 [astro-ph.EP].
- Booth, R. A., and J. D. Ilee. 2019. Planet-forming material in a protoplanetary disc: the interplay between chemical evolution and pebble drift. *MNRAS* 487, no. 3 (August): 3998–4011. <https://doi.org/10.1093/mnras/stz1488>. arXiv: 1905.12639 [astro-ph.EP].
- Booth, Richard A., Cathie J. Clarke, Nikku Madhusudhan, and John D. Ilee. 2017. Chemical enrichment of giant planets and discs due to pebble drift. *MNRAS* 469, no. 4 (August): 3994–4011. <https://doi.org/10.1093/mnras/stx1103>. arXiv: 1705.03305 [astro-ph.EP].
- Bosman, A. D., A. J. Cridland, and Y. Miguel. 2019. Jupiter formed as a pebble pile around the N₂ ice line. *A&A* 632 (December): L11. <https://doi.org/10.1051/0004-6361/201936827>. arXiv: 1911.11154 [astro-ph.EP].
- Bosman, Arthur D., Alexander G. G. M. Tielens, and Ewine F. van Dishoeck. 2018. Efficiency of radial transport of ices in protoplanetary disks probed with infrared observations: the case of CO₂. *A&A* 611 (April): A80. <https://doi.org/10.1051/0004-6361/201732056>. arXiv: 1712.03989 [astro-ph.EP].
- Brown, Paul D., and S. B. Charnley. 1990. Chemical models of interstellar gas-grain processes. I. Modelling and the effect of accretion on gas abundances and mantle composition in dense clouds. *MNRAS* 244 (June): 432.
- Brown-Sevilla, S. B., M. Keppler, M. Barraza-Alfaro, J. D. Melon Fuksman, N. Kurtovic, P. Pinilla, M. Feldt, et al. 2021. A multiwavelength analysis of the spiral arms in the protoplanetary disk around WaOph 6. *A&A* 654 (October): A35. <https://doi.org/10.1051/0004-6361/202140783>. arXiv: 2107.13560 [astro-ph.EP].
- Carrera, Daniel, Anders Johansen, and Melvyn B. Davies. 2015. How to form planetesimals from mm-sized chondrules and chondrule aggregates. *A&A* 579 (July): A43. <https://doi.org/10.1051/0004-6361/201425120>. arXiv: 1501.05314 [astro-ph.EP].
- Cavalié, Thibault, Jonathan Lunine, Olivier Mousis, and Ricardo Hueso. 2024. The Deep Oxygen Abundance in Solar System Giant Planets, with a New Derivation for Saturn. *Space Sci. Rev.* 220, no. 1 (January): 8. <https://doi.org/10.1007/s11214-024-01045-6>. arXiv: 2407.07515 [astro-ph.EP].
- Changeat, Q., B. Edwards, A. F. Al-Refaie, A. Tsiaras, J. W. Skinner, J. Y. K. Cho, K. H. Yip, et al. 2022. Five Key Exoplanet Questions Answered via the Analysis of 25 Hot-Jupiter Atmospheres in Eclipse. *ApJS* 260, no. 1 (May): 3. <https://doi.org/10.3847/1538-4365/ac5cc2>. arXiv: 2204.11729 [astro-ph.EP].

- Cleeves, L. Ilseidore, Karin I. Öberg, David J. Wilner, Jane Huang, Ryan A. Loomis, Sean M. Andrews, and V. V. Guzman. 2018. Constraining Gas-phase Carbon, Oxygen, and Nitrogen in the IM Lup Protoplanetary Disk. *ApJ* 865, no. 2 (October): 155. <https://doi.org/10.3847/1538-4357/aade96>. arXiv: 1808.10682 [astro-ph.SR].
- Connelley, Michael S., and Bo Reipurth. 2018. A Near-infrared Spectroscopic Survey of FU Orionis Objects. *ApJ* 861, no. 2 (July): 145. <https://doi.org/10.3847/1538-4357/aaba7b>. arXiv: 1806.08880 [astro-ph.SR].
- Cridland, Alex J., Ewine F. van Dishoeck, Matthew Alessi, and Ralph E. Pudritz. 2019. Connecting planet formation and astrochemistry. A main sequence for C/O in hot exoplanetary atmospheres. *A&A* 632 (December): A63. <https://doi.org/10.1051/0004-6361/201936105>. arXiv: 1910.13171 [astro-ph.EP].
- . 2020. Connecting planet formation and astrochemistry. C/Os and N/Os of warm giant planets and Jupiter analogues. *A&A* 642 (October): A229. <https://doi.org/10.1051/0004-6361/202038767>. arXiv: 2009.02907 [astro-ph.EP].
- Cridland, Alexander J., Arthur D. Bosman, and Ewine F. van Dishoeck. 2020. Impact of vertical gas accretion on the carbon-to-oxygen ratio of gas giant atmospheres. *A&A* 635 (March): A68. <https://doi.org/10.1051/0004-6361/201936858>. arXiv: 2001.05808 [astro-ph.EP].
- Cridland, Alexander J., Christian Eistrup, and Ewine F. van Dishoeck. 2019. Connecting planet formation and astrochemistry. Refractory carbon depletion leading to super-stellar C/O in giant planetary atmospheres. *A&A* 627 (July): A127. <https://doi.org/10.1051/0004-6361/201834378>. arXiv: 1901.08896 [astro-ph.EP].
- Cuppen, H. M., C. Walsh, T. Lamberts, D. Semenov, R. T. Garrod, E. M. Pentead, and S. Ioppolo. 2017. Grain Surface Models and Data for Astrochemistry. *Space Sci. Rev.* 212, nos. 1-2 (October): 1-58. <https://doi.org/10.1007/s11214-016-0319-3>.
- Cuzzi, Jeffrey N., and Kevin J. Zahnle. 2004. Material Enhancement in Protoplanetary Nebulae by Particle Drift through Evaporation Fronts. *ApJ* 614, no. 1 (October): 490-496. <https://doi.org/10.1086/423611>. arXiv: astro-ph/0409276 [astro-ph].
- Danti, C., B. Bitsch, and J. Mah. 2023. Composition of giant planets: The roles of pebbles and planetesimals. *A&A* 679 (November): L7. <https://doi.org/10.1051/0004-6361/202347501>. arXiv: 2310.02886 [astro-ph.EP].
- Dawson, Rebekah I., and John Asher Johnson. 2018. Origins of Hot Jupiters. *ARA&A* 56 (September): 175-221. <https://doi.org/10.1146/annurev-astro-081817-051853>. arXiv: 1801.06117 [astro-ph.EP].
- Dong, Ruobing, Eduard Vorobyov, Yaroslav Pavlyuchenkov, Eugene Chiang, and Haiyu Baobab Liu. 2016. Signatures of Gravitational Instability in Resolved Images of Protostellar Disks. *ApJ* 823, no. 2 (June): 141. <https://doi.org/10.3847/0004-637X/823/2/141>. arXiv: 1603.01618 [astro-ph.SR].
- Draine, B. T. 1978. Photoelectric heating of interstellar gas. *ApJS* 36 (April): 595-619. <https://doi.org/10.1086/190513>.
- Drażkowska, J., and Y. Alibert. 2017. Planetesimal formation starts at the snow line. *A&A* 608 (December): A92. <https://doi.org/10.1051/0004-6361/201731491>. arXiv: 1710.00009 [astro-ph.EP].
- Dutrey, A., V. Wakelam, Y. Boehler, S. Guilloteau, F. Hersant, D. Semenov, E. Chapillon, et al. 2011. Chemistry in disks. V. Sulfur-bearing molecules in the protoplanetary disks surrounding LkCa15, MWC480, DM Tauri, and GO Tauri. *A&A* 535 (November): A104. <https://doi.org/10.1051/0004-6361/201116931>. arXiv: 1109.5870 [astro-ph.SR].
- Eistrup, Christian, Catherine Walsh, and Ewine F. van Dishoeck. 2016. Setting the volatile composition of (exo)planet-building material. Does chemical evolution in disk midplanes matter? *A&A* 595 (November): A83. <https://doi.org/10.1051/0004-6361/201628509>. arXiv: 1607.06710 [astro-ph.EP].
- . 2018. Molecular abundances and C/O ratios in chemically evolving planet-forming disk midplanes. *A&A* 613 (May): A14. <https://doi.org/10.1051/0004-6361/201731302>. arXiv: 1709.07863 [astro-ph.EP].
- Facchini, Stefano, Richard Teague, Jaehan Bae, Myriam Benisty, Miriam Keppler, and Andrea Isella. 2021. The Chemical Inventory of the Planet-hosting Disk PDS 70. *AJ* 162, no. 3 (September): 99. <https://doi.org/10.3847/1538-3881/abf0a4>. arXiv: 2101.08369 [astro-ph.EP].
- Fedele, D., and C. Favre. 2020. Measuring elemental abundance ratios in protoplanetary disks at millimeter wavelengths. *A&A* 638 (June): A110. <https://doi.org/10.1051/0004-6361/202037927>. arXiv: 2005.03891 [astro-ph.SR].
- Fraser, Helen J., Mark P. Collings, Martin R. S. McCoustra, and David A. Williams. 2001. Thermal desorption of water ice in the interstellar medium. *MNRAS* 327, no. 4 (November): 1165-1172. <https://doi.org/10.1046/j.1365-8711.2001.04835.x>. arXiv: astro-ph/0107487 [astro-ph].
- Fu, Guangwei, Luis Welbanks, Drake Deming, Julie Inglis, Michael Zhang, Joshua Lothringer, Jegug Ih, et al. 2024. Hydrogen sulfide and metal-enriched atmosphere for a Jupiter-mass exoplanet. *arXiv e-prints* (July): arXiv:2407.06163. <https://doi.org/10.48550/arXiv.2407.06163>. arXiv: 2407.06163 [astro-ph.EP].
- Gail, Hans-Peter, and Mario Trieloff. 2017. Spatial distribution of carbon dust in the early solar nebula and the carbon content of planetesimals. *A&A* 606 (September): A16. <https://doi.org/10.1051/0004-6361/201730480>. arXiv: 1707.07611 [astro-ph.EP].
- Gammie, Charles F. 1996. Layered Accretion in T Tauri Disks. *ApJ* 457 (January): 355. <https://doi.org/10.1086/176735>.
- Gárate, Matias, Til Birnstiel, Joanna Drażkowska, and Sebastian Markus Stammer. 2020. Gas accretion damped by dust back-reaction at the snow line. *A&A* 635 (March): A149. <https://doi.org/10.1051/0004-6361/201936067>. arXiv: 1906.07708 [astro-ph.EP].
- GRAVITY Collaboration, M. Nowak, S. Lacour, P. Mollière, J. Wang, B. Charney, E. F. van Dishoeck, et al. 2020. Peering into the formation history of β Pictoris b with VLTI/GRAVITY long-baseline interferometry. *A&A* 633 (January): A110. <https://doi.org/10.1051/0004-6361/201936898>. arXiv: 1912.04651 [astro-ph.EP].
- Gressel, Oliver, Neal J. Turner, Richard P. Nelson, and Colin P. McNally. 2015. Global Simulations of Protoplanetary Disks With Ohmic Resistivity and Ambipolar Diffusion. *ApJ* 801, no. 2 (March): 84. <https://doi.org/10.1088/0004-637X/801/2/84>. arXiv: 1501.05431 [astro-ph.EP].
- Gundlach, B., and J. Blum. 2015. The Stickiness of Micrometer-sized Water-ice Particles. *ApJ* 798, no. 1 (January): 34. <https://doi.org/10.1088/0004-637X/798/1/34>. arXiv: 1410.7199 [astro-ph.EP].
- Harrington Pinto, Olga, Maria Womack, Yanga Fernandez, and James Bauer. 2022. A Survey of CO, CO₂, and H₂O in Comets and Centaurs. *PSJ* 3, no. 11 (November): 247. <https://doi.org/10.3847/PSJ/ac960d>. arXiv: 2209.09985 [astro-ph.EP].
- Hartmann, L., and S. J. Kenyon. 1985. On the nature of FU Orionis objects. *ApJ* 299 (December): 462-478. <https://doi.org/10.1086/163713>.
- Hasegawa, T. I., and E. Herbst. 1993. Three-Phase Chemical Models of Dense Interstellar Clouds - Gas Dust Particle Mantles and Dust Particle Surfaces. *MNRAS* 263 (August): 589. <https://doi.org/10.1093/mnras/263.3.589>.
- Hensley, Brandon S., and B. T. Draine. 2021. Observational Constraints on the Physical Properties of Interstellar Dust in the Post-Planck Era. *ApJ* 906, no. 2 (January): 73. <https://doi.org/10.3847/1538-4357/abc8f1>. arXiv: 2009.00018 [astro-ph.GA].
- Hoch, Kielan K. W., Quinn M. Konopacky, Christopher A. Theissen, Jean-Baptiste Ruffio, Travis S. Barman, Emily L. Rickman, Marshall D. Perrin, Bruce Macintosh, and Christian Marois. 2023. Assessing the C/O Ratio Formation Diagnostic: A Potential Trend with Companion Mass. *AJ* 166, no. 3 (September): 85. <https://doi.org/10.3847/1538-3881/ace442>. arXiv: 2212.04557 [astro-ph.EP].

- Huang, Jane, Sean M. Andrews, Cornelis P. Dullemond, Andrea Isella, Laura M. Pérez, Viviana V. Guzmán, Karin I. Öberg, et al. 2018. The Disk Substructures at High Angular Resolution Project (DSHARP). II. Characteristics of Annular Substructures. *Apj* 869, no. 2 (December): L42. <https://doi.org/10.3847/2041-8213/aaf740>. arXiv: 1812.04041 [astro-ph.EP].
- Huang, Jane, Sean M. Andrews, Laura M. Pérez, Zhaohuan Zhu, Cornelis P. Dullemond, Andrea Isella, Myriam Benisty, et al. 2018. The Disk Substructures at High Angular Resolution Project (DSHARP). III. Spiral Structures in the Millimeter Continuum of the Elias 27, IM Lup, and WaOph 6 Disks. *Apj* 869, no. 2 (December): L43. <https://doi.org/10.3847/2041-8213/aaf7a0>. arXiv: 1812.04193 [astro-ph.SR].
- Huang, Jane, Edwin A. Bergin, Romane Le Gal, Sean M. Andrews, Jaehan Bae, Luke Keyte, and J. A. Sturm. 2024. Constraints on the gas-phase C/O ratio of DR Tau's outer disk from CS, SO, and C₂H observations. *arXiv e-prints* (July): arXiv:2407.01679. <https://doi.org/10.48550/arXiv.2407.01679>. arXiv: 2407.01679 [astro-ph.EP].
- Hyodo, Ryuki, Tristan Guillot, Shigeru Ida, Satoshi Okuzumi, and Andrew N. Youdin. 2021. Planetesimal formation around the snow line. II. Dust or pebbles? *A&A* 646 (February): A14. <https://doi.org/10.1051/0004-6361/202039894>. arXiv: 2012.06700 [astro-ph.EP].
- Ilee, J. D., A. C. Boley, P. Caselli, R. H. Durisen, T. W. Hartquist, and J. M. C. Rawlings. 2011. Chemistry in a gravitationally unstable protoplanetary disc. *MNRAS* 417, no. 4 (November): 2950–2961. <https://doi.org/10.1111/j.1365-2966.2011.19455.x>. arXiv: 1107.3041 [astro-ph.GA].
- Jiang, Haochang, and Chris W. Ormel. 2023. Efficient planet formation by pebble accretion in ALMA rings. *MNRAS* 518, no. 3 (January): 3877–3900. <https://doi.org/10.1093/mnras/stac3275>. arXiv: 2207.13002 [astro-ph.EP].
- Kadam, Kundan, Eduard Vorobyov, and Shantanu Basu. 2022. Primordial dusty rings and episodic outbursts in protoplanetary discs. *MNRAS* 516, no. 3 (November): 4448–4468. <https://doi.org/10.1093/mnras/stac2455>. arXiv: 2208.12105 [astro-ph.EP].
- Kadam, Kundan, Eduard Vorobyov, Zsolt Regály, Ágnes Kóspál, and Péter Ábrahám. 2019. Dynamical Gaseous Rings in Global Simulations of Protoplanetary Disk Formation. *Apj* 882, no. 2 (September): 96. <https://doi.org/10.3847/1538-4357/ab378a>. arXiv: 1908.02515 [astro-ph.SR].
- . 2020. Outbursts in Global Protoplanetary Disk Simulations. *Apj* 895, no. 1 (May): 41. <https://doi.org/10.3847/1538-4357/ab8bd8>. arXiv: 2005.03578 [astro-ph.SR].
- Kama, M., S. Bruderer, E. F. van Dishoeck, M. Hogerheijde, C. P. Folsom, A. Miotello, D. Fedele, A. Belloche, R. Güsten, and F. Wyrowski. 2016. Volatile-carbon locking and release in protoplanetary disks. A study of TW Hya and HD 100546. *A&A* 592 (August): A83. <https://doi.org/10.1051/0004-6361/201526991>. arXiv: 1605.05093 [astro-ph.EP].
- Khorshid, N., M. Min, and J. M. Désert. 2023. Retrieving planet formation parameters of WASP-77Ab using SimAb. *A&A* 675 (July): A95. <https://doi.org/10.1051/0004-6361/202245469>. arXiv: 2311.15702 [astro-ph.EP].
- Kratter, Kaidlin, and Giuseppe Lodato. 2016. Gravitational Instabilities in Circumstellar Disks. *ARA&A* 54 (September): 271–311. <https://doi.org/10.1146/annurev-astro-081915-023307>. arXiv: 1603.01280 [astro-ph.SR].
- Krijt, Sebastiaan, Arthur D. Bosman, Ke Zhang, Kamber R. Schwarz, Fred J. Ciesla, and Edwin A. Bergin. 2020. CO Depletion in Protoplanetary Disks: A Unified Picture Combining Physical Sequestration and Chemical Processing. *Apj* 899, no. 2 (August): 134. <https://doi.org/10.3847/1538-4357/aba75d>. arXiv: 2007.09517 [astro-ph.SR].
- Krijt, Sebastiaan, Kamber R. Schwarz, Edwin A. Bergin, and Fred J. Ciesla. 2018. Transport of CO in Protoplanetary Disks: Consequences of Pebble Formation, Settling, and Radial Drift. *Apj* 864, no. 1 (September): 78. <https://doi.org/10.3847/1538-4357/aad69b>. arXiv: 1808.01840 [astro-ph.EP].
- Lambrechts, M., and A. Johansen. 2012. Rapid growth of gas-giant cores by pebble accretion. *A&A* 544 (August): A32. <https://doi.org/10.1051/0004-6361/201219127>. arXiv: 1205.3030 [astro-ph.EP].
- Lee, Eve J., J. R. Fuentes, and Philip F. Hopkins. 2022. Establishing Dust Rings and Forming Planets within Them. *Apj* 937, no. 2 (October): 95. <https://doi.org/10.3847/1538-4357/ac8cfe>. arXiv: 2206.01219 [astro-ph.EP].
- Lee, Jeong-Eun, Edwin A. Bergin, and Hideko Nomura. 2010. The Solar Nebula on Fire: A Solution to the Carbon Deficit in the Inner Solar System. *Apj* 710, no. 1 (February): L21–L25. <https://doi.org/10.1088/2041-8205/710/1/L21>. arXiv: 1001.0818 [astro-ph.GA].
- Lee, Jeong-Eun, Seokho Lee, Giseon Baek, Yuri Aikawa, Lucas Cieza, Sung-Yong Yoon, Gregory Herczeg, Doug Johnstone, and Simon Casassus. 2019. The ice composition in the disk around V883 Ori revealed by its stellar outburst. *Nature Astronomy* 3 (February): 314–319. <https://doi.org/10.1038/s41550-018-0680-0>. arXiv: 1809.00353 [astro-ph.SR].
- Leemker, M., A. S. Booth, E. F. van Dishoeck, L. Wölfer, and B. Dent. 2024. Chemistry across dust and gas gaps in protoplanetary disks: modelling the co-spatial molecular rings in the HD 100546 disk. *arXiv e-prints* (May): arXiv:2405.10361. <https://doi.org/10.48550/arXiv.2405.10361>. arXiv: 2405.10361 [astro-ph.EP].
- Lenz, Christian T., Hubert Klahr, and Tilman Birnstiel. 2019. Planetesimal Population Synthesis: Pebble Flux-regulated Planetesimal Formation. *Apj* 874, no. 1 (March): 36. <https://doi.org/10.3847/1538-4357/ab05d9>. arXiv: 1902.07089 [astro-ph.EP].
- Li, Cheng, Michael Allison, Sushil Atreya, Shawn Brueshaber, Leigh N. Fletcher, Tristan Guillot, Liming Li, et al. 2024. Super-adiabatic temperature gradient at Jupiter's equatorial zone and implications for the water abundance. *Icarus* 414 (May): 116028. <https://doi.org/10.1016/j.icarus.2024.116028>. arXiv: 2403.05363 [astro-ph.EP].
- Li, Rixin, and Andrew N. Youdin. 2021. Thresholds for Particle Clumping by the Streaming Instability. *Apj* 919, no. 2 (October): 107. <https://doi.org/10.3847/1538-4357/ac0e9f>. arXiv: 2105.06042 [astro-ph.EP].
- Ligterink, N. F. W., K. A. Kipper, and S. Gavino. 2024. Mind the Trap: Non-negligible effect of volatile trapping in ice on C/O ratios in protoplanetary disks and exoplanetary atmospheres. *arXiv e-prints* (June): arXiv:2406.16029. <https://doi.org/10.48550/arXiv.2406.16029>. arXiv: 2406.16029 [astro-ph.EP].
- Lin, D. N. C., P. Bodenheimer, and D. C. Richardson. 1996. Orbital migration of the planetary companion of 51 Pegasi to its present location. *Nature* 380, no. 6575 (April): 606–607. <https://doi.org/10.1038/380606a0>.
- Line, Michael R., Matteo Brogi, Jacob L. Bean, Siddharth Gandhi, Joseph Zalesky, Vivien Parmentier, Peter Smith, et al. 2021. A solar C/O and sub-solar metallicity in a hot Jupiter atmosphere. *Nature* 598, no. 7882 (October): 580–584. <https://doi.org/10.1038/s41586-021-03912-6>. arXiv: 2110.14821 [astro-ph.EP].
- Lodders, Katharina. 2004. Jupiter Formed with More Tar than Ice. *Apj* 611, no. 1 (August): 587–597. <https://doi.org/10.1086/421970>.
- Long, Feng, Paola Pinilla, Gregory J. Herczeg, Daniel Harsono, Giovanni Dipierro, Ilaria Pascucci, Nathan Hendler, et al. 2018. Gaps and Rings in an ALMA Survey of Disks in the Taurus Star-forming Region. *Apj* 869, no. 1 (December): 17. <https://doi.org/10.3847/1538-4357/aae8e1>. arXiv: 1810.06044 [astro-ph.SR].
- Madhusudhan, Nikku. 2012. C/O Ratio as a Dimension for Characterizing Exoplanetary Atmospheres. *Apj* 758, no. 1 (October): 36. <https://doi.org/10.1088/0004-637X/758/1/36>. arXiv: 1209.2412 [astro-ph.EP].

- Madhusudhan, Nikku, Joseph Harrington, Kevin B. Stevenson, Sarah Nymeyer, Christopher J. Campo, Peter J. Wheatley, Drake Deming, et al. 2011. A high C/O ratio and weak thermal inversion in the atmosphere of exoplanet WASP-12b. *Nature* 469, no. 7328 (January): 64–67. <https://doi.org/10.1038/nature09602>. arXiv: 1012.1603 [astro-ph.EP].
- Matter, A., F. C. Pignatale, and B. Lopez. 2020. Spatially resolving the chemical composition of the planet building blocks. *MNRAS* 497, no. 3 (September): 2540–2552. <https://doi.org/10.1093/mnras/staa2137>. arXiv: 2007.09385 [astro-ph.EP].
- McKay, Adam J., Michael A. DiSanti, Michael S. P. Kelley, Matthew M. Knight, Maria Womack, Kacper Wierzchos, Olga Harrington Pinto, et al. 2019. The Peculiar Volatile Composition of CO-dominated Comet C/2016 R2 (PanSTARRS). *AJ* 158, no. 3 (September): 128. <https://doi.org/10.3847/1538-3881/ab32e4>. arXiv: 1907.07208 [astro-ph.EP].
- Meru, Farzana, and Matthew R. Bate. 2010. Exploring the conditions required to form giant planets via gravitational instability in massive protoplanetary discs. *MNRAS* 406, no. 4 (August): 2279–2288. <https://doi.org/10.1111/j.1365-2966.2010.16867.x>. arXiv: 1004.3766 [astro-ph.EP].
- Meru, Farzana, Attila Juhász, John D. Ilee, Cathie J. Clarke, Giovanni P. Rosotti, and Richard A. Booth. 2017. On the Origin of the Spiral Morphology in the Elias 2-27 Circumstellar Disk. *ApJ* 839, no. 2 (April): L24. <https://doi.org/10.3847/2041-8213/aa6837>. arXiv: 1703.05338 [astro-ph.EP].
- Minissale, Marco, Yuri Aikawa, Edwin Bergin, Mathieu Bertin, Wendy A. Brown, Stephanie Cazaux, Steven B. Charnley, et al. 2022. Thermal Desorption of Interstellar Ices: A Review on the Controlling Parameters and Their Implications from Snowlines to Chemical Complexity. *ACS Earth and Space Chemistry* 6, no. 3 (March): 597–630. <https://doi.org/10.1021/acsearthspacechem.1c00357>. arXiv: 2201.07512 [astro-ph.GA].
- Miotello, A., S. Facchini, E. F. van Dishoeck, P. Cazzoletti, L. Testi, J. P. Williams, M. Ansdell, S. van Terwisga, and N. van der Marel. 2019. Bright C₂H emission in protoplanetary discs in Lupus: high volatile C/O > 1 ratios. *A&A* 631 (November): A69. <https://doi.org/10.1051/0004-6361/201935441>. arXiv: 1909.04477 [astro-ph.SR].
- Mollière, P., T. Stolker, S. Lacour, G. P. P. L. Otten, J. Shangguan, B. Charney, T. Molyarova, et al. 2020. Retrieving scattering clouds and disequilibrium chemistry in the atmosphere of HR 8799e. *A&A* 640 (August): A131. <https://doi.org/10.1051/0004-6361/202038325>. arXiv: 2006.09394 [astro-ph.EP].
- Mollière, Paul, Tamara Molyarova, Bertram Bitsch, Thomas Henning, Aaron Schneider, Laura Kreidberg, Christian Eistrup, et al. 2022. Interpreting the Atmospheric Composition of Exoplanets: Sensitivity to Planet Formation Assumptions. *ApJ* 934, no. 1 (July): 74. <https://doi.org/10.3847/1538-4357/ac6a56>. arXiv: 2204.13714 [astro-ph.EP].
- Molyarova, Tamara, Vitaly Akimkin, Dmitry Semenov, Thomas Henning, Anton Vasyunin, and Dmitri Wiebe. 2017. Gas Mass Tracers in Protoplanetary Disks: CO is Still the Best. *ApJ* 849, no. 2 (November): 130. <https://doi.org/10.3847/1538-4357/aa9227>. arXiv: 1710.02993 [astro-ph.EP].
- Molyarova, Tamara, Eduard I. Vorobyov, Vitaly Akimkin, Aleksandr Skliarevskii, Dmitri Wiebe, and Manuel Güdel. 2021. Gravito-viscous Protoplanetary Disks with a Dust Component. V. The Dynamic Model for Freeze-out and Sublimation of Volatiles. *ApJ* 910, no. 2 (April): 153. <https://doi.org/10.3847/1538-4357/abe2b0>. arXiv: 2103.06045 [astro-ph.EP].
- Morbideilli, A., J. Szulágyi, A. Crida, E. Lega, B. Bitsch, T. Tanigawa, and K. Kanagawa. 2014. Meridional circulation of gas into gaps opened by giant planets in three-dimensional low-viscosity disks. *Icarus* 232 (April): 266–270. <https://doi.org/10.1016/j.icarus.2014.01.010>. arXiv: 1401.2925 [astro-ph.EP].
- Mordasini, C., R. van Boekel, P. Mollière, Th. Henning, and Björn Benneke. 2016. The Imprint of Exoplanet Formation History on Observable Present-day Spectra of Hot Jupiters. *ApJ* 832, no. 1 (November): 41. <https://doi.org/10.3847/0004-637X/832/1/41>. arXiv: 1609.03019 [astro-ph.EP].
- Moses, J. I., N. Madhusudhan, C. Visscher, and R. S. Freedman. 2013. Chemical Consequences of the C/O Ratio on Hot Jupiters: Examples from WASP-12b, CoRoT-2b, XO-1b, and HD 189733b. *ApJ* 763, no. 1 (January): 25. <https://doi.org/10.1088/0004-637X/763/1/25>. arXiv: 1211.2996 [astro-ph.EP].
- Mousis, Olivier, Sarah E. Anderson, Adrienn Luszpay-Kuti, Kathleen E. Mandt, and Pierre Vernazza. 2024. Triton and Pluto: same origin but separated at birth. *arXiv e-prints* (June): arXiv:2406.03815. <https://doi.org/10.48550/arXiv.2406.03815>. arXiv: 2406.03815 [astro-ph.EP].
- Mousis, Olivier, Thibault Cavalié, Jonathan I. Lunine, Kathleen E. Mandt, Ricardo Hueso, Artyom Aguichine, Antoine Schneeberger, et al. 2024. Recipes for Forming a Carbon-Rich Giant Planet. *Space Sci. Rev.* 220, no. 4 (June): 44. <https://doi.org/10.1007/s11214-024-01071-4>. arXiv: 2405.19748 [astro-ph.EP].
- Nasedkin, E., P. Mollière, S. Lacour, M. Nowak, L. Kreidberg, T. Stolker, J. J. Wang, et al. 2024. Four-of-a-kind? Comprehensive atmospheric characterisation of the HR 8799 planets with VLTI/GRAVITY. *arXiv e-prints* (April): arXiv:2404.03776. <https://doi.org/10.48550/arXiv.2404.03776>. arXiv: 2404.03776 [astro-ph.EP].
- Nayakshin, Sergei. 2010a. Formation of planets by tidal downsizing of giant planet embryos. *MNRAS* 408, no. 1 (October): L36–L40. <https://doi.org/10.1111/j.1745-3933.2010.00923.x>. arXiv: 1007.4159 [astro-ph.EP].
- . 2010b. Grain sedimentation inside giant planet embryos. *MNRAS* 408, no. 4 (November): 2381–2396. <https://doi.org/10.1111/j.1365-2966.2010.17289.x>. arXiv: 1007.4162 [astro-ph.EP].
- Nayakshin, Sergei, Ravit Helled, and Aaron C. Boley. 2014. Core-assisted gas capture instability: a new mode of giant planet formation by gravitationally unstable discs. *MNRAS* 440, no. 4 (June): 3797–3808. <https://doi.org/10.1093/mnras/stu473>. arXiv: 1403.1813 [astro-ph.EP].
- Nortmann, L., F. Lesjak, F. Yan, D. Cont, S. Czesla, A. Lavail, A. D. Rains, et al. 2024. CRIRES+ transmission spectroscopy of WASP-127b. Detection of the resolved signatures of a supersonic equatorial jet and cool poles in a hot planet. *arXiv e-prints* (April): arXiv:2404.12363. <https://doi.org/10.48550/arXiv.2404.12363>. arXiv: 2404.12363 [astro-ph.EP].
- Öberg, K. I., F. van Broekhuizen, H. J. Fraser, S. E. Bisschop, E. F. van Dishoeck, and S. Schlemmer. 2005. Competition between CO and N₂ Desorption from Interstellar Ices. *ApJ* 621, no. 1 (March): L33–L36. <https://doi.org/10.1086/428901>.
- Öberg, Karin I., A. C. Adwin Boogert, Klaus M. Pontoppidan, Saskia van den Broek, Ewine F. van Dishoeck, Sandrine Bottinelli, Geoffrey A. Blake, and II Evans Neal J. 2011. The Spitzer Ice Legacy: Ice Evolution from Cores to Protostars. *ApJ* 740, no. 2 (October): 109. <https://doi.org/10.1088/0004-637X/740/2/109>. arXiv: 1107.5825 [astro-ph.GA].
- Öberg, Karin I., Ruth Murray-Clay, and Edwin A. Bergin. 2011. The Effects of Snowlines on C/O in Planetary Atmospheres. *ApJ* 743, no. 1 (December): L16. <https://doi.org/10.1088/2041-8205/743/1/L16>. arXiv: 1110.5567 [astro-ph.GA].
- Öberg, Karin I., and Robin Wordsworth. 2019. Jupiter’s Composition Suggests its Core Assembled Exterior to the N₂ Snowline. *AJ* 158, no. 5 (November): 194. <https://doi.org/10.3847/1538-3881/ab46a8>. arXiv: 1909.11246 [astro-ph.EP].
- Ohno, Kazumasa, and Takahiro Ueda. 2021. Jupiter’s “cold” formation in the protosolar disk shadow. An explanation for the planet’s uniformly enriched atmosphere. *A&A* 651 (July): L2. <https://doi.org/10.1051/0004-6361/202141169>. arXiv: 2106.09084 [astro-ph.EP].

- Okuzumi, Satoshi, and Shigenobu Hirose. 2011. Modeling Magnetorotational Turbulence in Protoplanetary Disks with Dead Zones. *Apj* 742, no. 2 (December): 65. <https://doi.org/10.1088/0004-637X/742/2/65>. arXiv: 1108.4892 [astro-ph.EP].
- Okuzumi, Satoshi, and Ryo Tazaki. 2019. Nonsticky Ice at the Origin of the Uniformly Polarized Submillimeter Emission from the HL Tau Disk. *Apj* 878, no. 2 (June): 132. <https://doi.org/10.3847/1538-4357/ab204d>. arXiv: 1904.03869 [astro-ph.EP].
- Ootsubo, Takafumi, Hideyo Kawakita, Saki Hamada, Hitomi Kobayashi, Mitsuru Yamaguchi, Fumihiko Usui, Takao Nakagawa, et al. 2012. AKARI Near-infrared Spectroscopic Survey for CO₂ in 18 Comets. *Apj* 752, no. 1 (June): 15. <https://doi.org/10.1088/0004-637X/752/1/15>.
- Padoan, Paolo, Liubin Pan, Veli-Matti Pelkonen, Troels Haugboelle, and AAKE Nordlund. 2024. Protoplanetary Disks from Pre-Main Sequence Bondi-Hoyle Accretion. *arXiv e-prints* (May): arXiv:2405.07334. <https://doi.org/10.48550/arXiv.2405.07334>. arXiv: 2405.07334 [astro-ph.GA].
- Padovani, M., D. Galli, and A. E. Glassgold. 2009. Cosmic-ray ionization of molecular clouds. *A&A* 501, no. 2 (July): 619–631. <https://doi.org/10.1051/0004-6361/200911794>. arXiv: 0904.4149 [astro-ph.SR].
- Pavlyuchenkov, Yaroslav, Vitaly Akimkin, Dmitri Wiebe, and Eduard Vorobyov. 2019. Revealing dust segregation in protoplanetary discs with the help of multifrequency spectral index maps. *MNRAS* 486, no. 3 (July): 3907–3914. <https://doi.org/10.1093/mnras/stz1046>. arXiv: 1904.05251 [astro-ph.IM].
- Pelkonen, Veli-Matti, Paolo Padoan, Mika Juvela, Troels Haugbølle, and Åke Nordlund. 2024. Origin and Evolution of Angular Momentum of Class II Disks. *arXiv e-prints* (May): arXiv:2405.06520. <https://doi.org/10.48550/arXiv.2405.06520>. arXiv: 2405.06520 [astro-ph.SR].
- Pérez, Laura M., John M. Carpenter, Sean M. Andrews, Luca Ricci, Andrea Isella, Hendrik Linz, Anneila I. Sargent, et al. 2016. Spiral density waves in a young protoplanetary disk. *Science* 353, no. 6307 (September): 1519–1521. <https://doi.org/10.1126/science.aaf8296>. arXiv: 1610.05139 [astro-ph.GA].
- Piso, Ana-Maria A., Karin I. Öberg, Tilman Birnstiel, and Ruth A. Murray-Clay. 2015. C/O and Snowline Locations in Protoplanetary Disks: The Effect of Radial Drift and Viscous Gas Accretion. *Apj* 815, no. 2 (December): 109. <https://doi.org/10.1088/0004-637X/815/2/109>. arXiv: 1511.05563 [astro-ph.EP].
- Pontoppidan, K. M., C. Salyk, E. A. Bergin, S. Brittain, B. Marty, O. Mousis, and K. I. Öberg. 2014. Volatiles in Protoplanetary Disks. In *Protostars and planets vi*, edited by Henrik Beuther, Ralf S. Klessen, Cornelis P. Dullemond, and Thomas Henning, 363–385. January. https://doi.org/10.2458/azu_uapress_9780816531240-ch016. arXiv: 1401.2423 [astro-ph.EP].
- Przybilla, Norbert, Maria-Fernanda Nieva, and Keith Butler. 2008. A Cosmic Abundance Standard: Chemical Homogeneity of the Solar Neighborhood and the ISM Dust-Phase Composition. *Apj* 688, no. 2 (December): L103. <https://doi.org/10.1086/595618>. arXiv: 0809.2403 [astro-ph].
- Rafikov, Roman R. 2005. Can Giant Planets Form by Direct Gravitational Instability? *Apj* 621, no. 1 (March): L69–L72. <https://doi.org/10.1086/428899>. arXiv: astro-ph/0406469 [astro-ph].
- Rampinelli, L., S. Facchini, M. Leemker, J. Bae, M. Benisty, R. Teague, C. J. Law, K. I. Öberg, B. Portilla-Revelo, and A. J. Cridland. 2024. ALMA high-resolution observations unveil planet formation shaping molecular emission in the PDS 70 disk. *arXiv e-prints* (July): arXiv:2407.06272. <https://doi.org/10.48550/arXiv.2407.06272>. arXiv: 2407.06272 [astro-ph.EP].
- Reggiani, Henrique, Jhon Yana Galarza, Kevin C. Schlaufman, David K. Sing, Brian F. Healy, Andrew McWilliam, Joshua D. Lothringer, and Laurent Pueyo. 2024. Insight into the Formation of β Pic b through the Composition of Its Parent Protoplanetary Disk as Revealed by the β Pic Moving Group Member HD 181327. *AJ* 167, no. 1 (January): 45. <https://doi.org/10.3847/1538-3881/ad0f93>. arXiv: 2311.12210 [astro-ph.SR].
- Schneider, Aaron David, and Bertram Bitsch. 2021. How drifting and evaporating pebbles shape giant planets. I. Heavy element content and atmospheric C/O. *A&A* 654 (October): A71. <https://doi.org/10.1051/0004-6361/202039640>. arXiv: 2105.13267 [astro-ph.EP].
- Seager, S., L. J. Richardson, B. M. S. Hansen, K. Menou, J. Y. -K. Cho, and D. Deming. 2005. On the Dayside Thermal Emission of Hot Jupiters. *Apj* 632, no. 2 (October): 1122–1131. <https://doi.org/10.1086/444411>. arXiv: astro-ph/0504212 [astro-ph].
- Seligman, Darryl Z., Leslie A. Rogers, Samuel H. C. Cabot, John W. Noonan, Theodore Kareta, Kathleen E. Mandt, Fred Ciesla, et al. 2022. The Volatile Carbon-to-oxygen Ratio as a Tracer for the Formation Locations of Interstellar Comets. *PSJ* 3, no. 7 (July): 150. <https://doi.org/10.3847/PSJ/ac75b5>. arXiv: 2204.13211 [astro-ph.EP].
- Semenov, D., C. Favre, D. Fedele, S. Guilloteau, R. Teague, Th. Henning, A. Dutrey, E. Chapillon, F. Hersant, and V. Piétu. 2018. Chemistry in disks. XI. Sulfur-bearing species as tracers of protoplanetary disk physics and chemistry: the DM Tau case. *A&A* 617 (September): A28. <https://doi.org/10.1051/0004-6361/201832980>. arXiv: 1806.07707 [astro-ph.GA].
- Semenov, D., Th. Henning, Ch. Helling, M. Ilgner, and E. Sedlmayr. 2003. Rosseland and Planck mean opacities for protoplanetary discs. *A&A* 410 (November): 611–621. <https://doi.org/10.1051/0004-6361:20031279>. arXiv: astro-ph/0308344 [astro-ph].
- Semenov, D., and D. Wiebe. 2011. Chemical Evolution of Turbulent Protoplanetary Disks and the Solar Nebula. *ApJS* 196, no. 2 (October): 25. <https://doi.org/10.1088/0067-0049/196/2/25>. arXiv: 1104.4358 [astro-ph.GA].
- Shakura, N. I., and R. A. Sunyaev. 1973. Black holes in binary systems. Observational appearance. *A&A* 24 (January): 337–355.
- Sing, David K., Zafar Rustamkulov, Daniel P. Thorngren, Joanna K. Barstow, Pascal Tremblin, Catarina Alves de Oliveira, Tracy L. Beck, et al. 2024. A warm Neptune's methane reveals core mass and vigorous atmospheric mixing. *arXiv e-prints* (May): arXiv:2405.11027. <https://doi.org/10.48550/arXiv.2405.11027>. arXiv: 2405.11027 [astro-ph.EP].
- Smith, Peter C. B., Michael R. Line, Jacob L. Bean, Matteo Brogi, Prune August, Luis Welbanks, Jean-Michel Desert, et al. 2024. A Combined Ground-based and JWST Atmospheric Retrieval Analysis: Both IGRINS and NIRSpec Agree that the Atmosphere of WASP-77A b Is Metal-poor. *AJ* 167, no. 3 (March): 110. <https://doi.org/10.3847/1538-3881/ad17bf>. arXiv: 2312.13069 [astro-ph.EP].
- Stammler, Sebastian Markus, Tilman Birnstiel, Olja Panić, Cornelis Petrus Dullemond, and Carsten Dominik. 2017. Redistribution of CO at the location of the CO ice line in evolving gas and dust disks. *A&A* 600 (April): A140. <https://doi.org/10.1051/0004-6361/201629041>. arXiv: 1701.02385 [astro-ph.EP].
- Stevenson, David J., and Jonathan I. Lunine. 1988. Rapid formation of Jupiter by diffusive redistribution of water vapor in the solar nebula. *Icarus* 75, no. 1 (July): 146–155. [https://doi.org/10.1016/0019-1035\(88\)90133-9](https://doi.org/10.1016/0019-1035(88)90133-9).
- Swain, M. R., G. Tinetti, G. Vasisht, P. Deroo, C. Griffith, J. Bouwman, Pin Chen, et al. 2009. Water, Methane, and Carbon Dioxide Present in the Dayside Spectrum of the Exoplanet HD 209458b. *Apj* 704, no. 2 (October): 1616–1621. <https://doi.org/10.1088/0004-637X/704/2/1616>. arXiv: 0908.4010 [astro-ph.EP].

- Testi, L., T. Birnstiel, L. Ricci, S. Andrews, J. Blum, J. Carpenter, C. Dominik, et al. 2014. Dust Evolution in Protoplanetary Disks. In *Protostars and planets vi*, edited by Henrik Beuther, Ralf S. Klessen, Cornelis P. Dullemond, and Thomas Henning, 339–361. January. https://doi.org/10.2458/azu_uapress_9780816531240-ch015. arXiv: 1402.1354 [astro-ph.SR].
- Thiabaud, A., U. Marboeuf, Y. Alibert, I. Leya, and K. Mezger. 2015. Gas composition of the main volatile elements in protoplanetary discs and its implication for planet formation. *A&A* 574 (February): A138. <https://doi.org/10.1051/0004-6361/201424868>.
- Thies, Ingo, Pavel Kroupa, Simon P. Goodwin, Dimitrios Stamatellos, and Anthony P. Whitworth. 2010. Tidally Induced Brown Dwarf and Planet Formation in Circumstellar Disks. *ApJ* 717, no. 1 (July): 577–585. <https://doi.org/10.1088/0004-637X/717/1/577>. arXiv: 1005.3017 [astro-ph.SR].
- Tielens, A. G. G. M. 2005. *The Physics and Chemistry of the Interstellar Medium*.
- Tong, Simin, Richard Alexander, and Giovanni Rosotti. 2024. A question of personalities: evolution of viscous and wind-driven protoplanetary discs in the presence of dead zones. *MNRAS* (July). <https://doi.org/10.1093/mnras/stae1748>. arXiv: 2407.12209 [astro-ph.EP].
- Toomre, A. 1964. On the gravitational stability of a disk of stars. *ApJ* 139 (May): 1217–1238. <https://doi.org/10.1086/147861>.
- Topchieva, A., T. Molyarova, V. Akimkin, L. Maksimova, and E. Vorobyov. 2024. Ices on pebbles in protoplanetary discs. *MNRAS* 530, no. 3 (May): 2731–2748. <https://doi.org/10.1093/mnras/stae597>. arXiv: 2403.02895 [astro-ph.EP].
- Turrini, D., E. Schisano, S. Fonte, S. Molinari, R. Politi, D. Fedele, O. Panić, M. Kama, Q. Changeat, and G. Tinetti. 2021. Tracing the Formation History of Giant Planets in Protoplanetary Disks with Carbon, Oxygen, Nitrogen, and Sulfur. *ApJ* 909, no. 1 (March): 40. <https://doi.org/10.3847/1538-4357/abd6e5>. arXiv: 2012.14315 [astro-ph.EP].
- Umeybayashi, T., and T. Nakano. 1981. Fluxes of Energetic Particles and the Ionization Rate in Very Dense Interstellar Clouds. *PASJ* 33 (January): 617.
- Vallet, David, Anna C. Childs, Rebecca G. Martin, Mario Livio, and Stephen Lepp. 2023. Formation of super-Earths in icy dead zones around low-mass stars. *MNRAS* 519, no. 1 (February): L10–L14. <https://doi.org/10.1093/mnras/slac144>. arXiv: 2211.07759 [astro-ph.EP].
- Visser, R., E. F. van Dishoeck, S. D. Doty, and C. P. Dullemond. 2009. The chemical history of molecules in circumstellar disks. I. Ices. *A&A* 495, no. 3 (March): 881–897. <https://doi.org/10.1051/0004-6361/200810846>. arXiv: 0901.1313 [astro-ph.SR].
- Vorobyov, E. I. 2013. Formation of giant planets and brown dwarfs on wide orbits. *A&A* 552 (April): A129. <https://doi.org/10.1051/0004-6361/201220601>. arXiv: 1302.1892 [astro-ph.EP].
- Vorobyov, Eduard I., Vitaly Akimkin, Olga Stoyanovskaya, Yaroslav Pavlyuchenkov, and Haiyu Baobab Liu. 2018. Early evolution of viscous and self-gravitating circumstellar disks with a dust component. *A&A* 614 (June): A98. <https://doi.org/10.1051/0004-6361/201731690>. arXiv: 1801.06898 [astro-ph.EP].
- Vorobyov, Eduard I., and Shantanu Basu. 2010. The Burst Mode of Accretion and Disk Fragmentation in the Early Embedded Stages of Star Formation. *ApJ* 719, no. 2 (August): 1896–1911. <https://doi.org/10.1088/0004-637X/719/2/1896>. arXiv: 1007.2993 [astro-ph.SR].
- Vorobyov, Eduard I., and Vardan G. Elbakyan. 2019. Gravitoviscous protoplanetary disks with a dust component. II. Spatial distribution and growth of dust in a clumpy disk. *A&A* 631 (November): A1. <https://doi.org/10.1051/0004-6361/201936132>. arXiv: 1908.10589 [astro-ph.SR].
- Vorobyov, Eduard I., Vardan G. Elbakyan, Michihiro Takami, and Haiyu B. Liu. 2020. Effect of luminosity outbursts on protoplanetary disk dynamics. *A&A* 643 (November): A13. <https://doi.org/10.1051/0004-6361/202038122>. arXiv: 2009.01888 [astro-ph.SR].
- Vorobyov, Eduard I., Sergey Khaibrakhmanov, Shantanu Basu, and Marc Audard. 2020. Accretion bursts in magnetized gas-dust protoplanetary disks. *A&A* 644 (December): A74. <https://doi.org/10.1051/0004-6361/202039081>. arXiv: 2011.00951 [astro-ph.SR].
- Vorobyov, Eduard I., D. N. C. Lin, and Manuel Guedel. 2015. The effect of external environment on the evolution of protostellar disks. *A&A* 573 (January): A5. <https://doi.org/10.1051/0004-6361/201424583>. arXiv: 1410.1743 [astro-ph.SR].
- Vorobyov, Eduard I., Zsolt Regaly, Manuel Guedel, and Doug N. C. Lin. 2016. An alternative model for the origin of gaps in circumstellar disks. *A&A* 587 (March): A146. <https://doi.org/10.1051/0004-6361/201527701>. arXiv: 1601.08089 [astro-ph.SR].
- Vorobyov, Eduard I., Aleksandr M. Skliarevskii, Manuel Guedel, and Tamara Molyarova. 2024. Primordial dust rings, hidden dust mass, and the first generation of planetesimals in gravitationally unstable protoplanetary disks. *arXiv e-prints* (April): arXiv:2404.16151. <https://doi.org/10.48550/arXiv.2404.16151>. arXiv: 2404.16151 [astro-ph.EP].
- Vorobyov, Eduard I., Aleksandr M. Skliarevskii, Tamara Molyarova, Vitaly Akimkin, Yaroslav Pavlyuchenkov, Ágnes Kóspál, Haiyu Baobab Liu, Michihiro Takami, and Anastasiia Topchieva. 2022. Evolution of dust in protoplanetary disks of eruptive stars. *A&A* 658 (February): A191. <https://doi.org/10.1051/0004-6361/202141932>. arXiv: 2112.06004 [astro-ph.EP].
- Vorobyov, Eduard I., Olga V. Zakhzhay, and Michael M. Dunham. 2013. Fragmenting protostellar discs: properties and observational signatures. *MNRAS* 433, no. 4 (August): 3256–3273. <https://doi.org/10.1093/mnras/stt970>. arXiv: 1306.4074 [astro-ph.SR].
- Wada, Koji, Hidekazu Tanaka, Toru Suyama, Hiroshi Kimura, and Tetsuo Yamamoto. 2009. Collisional Growth Conditions for Dust Aggregates. *ApJ* 702, no. 2 (September): 1490–1501. <https://doi.org/10.1088/0004-637X/702/2/1490>.
- Walsh, Catherine, Hideko Nomura, and Ewine van Dishoeck. 2015. The molecular composition of the planet-forming regions of protoplanetary disks across the luminosity regime. *A&A* 582 (October): A88. <https://doi.org/10.1051/0004-6361/201526751>. arXiv: 1507.08544 [astro-ph.EP].
- Weber, Philipp, Sebastián Pérez, Alice Zurlo, James Miley, Antonio Hales, Lucas Cieza, David Principe, et al. 2023. Spirals and Clumps in V960 Mon: Signs of Planet Formation via Gravitational Instability around an FU Ori Star? *ApJ* 952, no. 1 (July): L17. <https://doi.org/10.3847/2041-8213/ace186>. arXiv: 2307.13433 [astro-ph.EP].
- Wei, Chen-En, Hideko Nomura, Jeong-Eun Lee, Wing-Huen Ip, Catherine Walsh, and T. J. Millar. 2019. The Effect of Carbon Grain Destruction on the Chemical Structure of Protoplanetary Disks. *ApJ* 870, no. 2 (January): 129. <https://doi.org/10.3847/1538-4357/aaf390>. arXiv: 1811.10194 [astro-ph.EP].
- Weidenschilling, S. J. 1977. Aerodynamics of solid bodies in the solar nebula. *MNRAS* 180 (July): 57–70. <https://doi.org/10.1093/mnras/180.2.57>.
- Weiner Mansfield, Megan, Michael R. Line, Joost P. Wardenier, Matteo Brogi, Jacob L. Bean, Hayley Beltz, Peter Smith, et al. 2024. The metallicity and carbon-to-oxygen ratio of the ultra-hot Jupiter WASP-76b from Gemini-S/IGRINS. *arXiv e-prints* (May): arXiv:2405.09769. <https://doi.org/10.48550/arXiv.2405.09769>. arXiv: 2405.09769 [astro-ph.EP].
- Westley, M. S., R. A. Baragiola, R. E. Johnson, and G. A. Baratta. 1995. Photodesorption from low-temperature water ice in interstellar and circumsolar grains. *Nature* 373, no. 6513 (February): 405–407. <https://doi.org/10.1038/373405a0>.
- Wierzbos, K., and M. Womack. 2018. C/2016 R2 (PANSTARRS): A Comet Rich in CO and Depleted in HCN. *AJ* 156, no. 1 (July): 34. <https://doi.org/10.3847/1538-3881/aac6bc>. arXiv: 1805.06918 [astro-ph.EP].

- Winter, Andrew J., Myriam Benisty, and Sean M. Andrews. 2024. Planet formation regulated by galactic-scale interstellar turbulence. *arXiv e-prints* (May): arXiv:2405.08451. arXiv: 2405.08451 [astro-ph.EP].
- Wong, Michael H., Paul R. Mahaffy, Sushil K. Atreya, Hasso B. Niemann, and Tobias C. Owen. 2004. Updated Galileo probe mass spectrometer measurements of carbon, oxygen, nitrogen, and sulfur on Jupiter. *Icarus* 171, no. 1 (September): 153–170. <https://doi.org/10.1016/j.icarus.2004.04.010>.
- Worthen, Kadin, Christine H. Chen, David R. Law, Cicero X. Lu, Kielan Hoch, Yiwei Chai, G. C. Sloan, et al. 2024. MIRI MRS Observations of β Pictoris. I. The Inner Dust, the Planet, and the Gas. *ApJ* 964, no. 2 (April): 168. <https://doi.org/10.3847/1538-4357/ad2354>.
- Xue, Qiao, Jacob L. Bean, Michael Zhang, Luis Welbanks, Jonathan Lunine, and Prune August. 2024. JWST Transmission Spectroscopy of HD 209458b: A Supersolar Metallicity, a Very Low C/O, and No Evidence of CH₄, HCN, or C₂H₂. *ApJ* 963, no. 1 (March): L5. <https://doi.org/10.3847/2041-8213/ad2682>. arXiv: 2310.03245 [astro-ph.EP].
- Yang, Chao-Chin, Anders Johansen, and Daniel Carrera. 2017. Concentrating small particles in protoplanetary disks through the streaming instability. *A&A* 606 (October): A80. <https://doi.org/10.1051/0004-6361/201630106>. arXiv: 1611.07014 [astro-ph.EP].
- Youdin, Andrew N., and Jeremy Goodman. 2005. Streaming Instabilities in Protoplanetary Disks. *ApJ* 620, no. 1 (February): 459–469. <https://doi.org/10.1086/426895>. arXiv: astro-ph/0409263 [astro-ph].
- Zhang, Yapeng, Ignas A. G. Snellen, Alexander J. Bohn, Paul Mollière, Christian Ginski, H. Jens Hoeijmakers, Matthew A. Kenworthy, et al. 2021. The ¹³CO-rich atmosphere of a young accreting super-Jupiter. *Nature* 595, no. 7867 (July): 370–372. <https://doi.org/10.1038/s41586-021-03616-x>. arXiv: 2107.06297 [astro-ph.EP].
- Zhu, Zhaohuan, Lee Hartmann, Charles F. Gammie, Laura G. Book, Jacob B. Simon, and Eric Engelhard. 2010. Long-term Evolution of Protostellar and Protoplanetary Disks. I. Outbursts. *ApJ* 713, no. 2 (April): 1134–1142. <https://doi.org/10.1088/0004-637X/713/2/1134>. arXiv: 1003.1759 [astro-ph.SR].
- Zhu, Zhaohuan, Yan-Fei Jiang, and James M. Stone. 2020. Global 3D radiation magnetohydrodynamic simulations for FU Ori's accretion disc and observational signatures of magnetic fields. *MNRAS* 495, no. 3 (January): 3494–3514. <https://doi.org/10.1093/mnras/staa952>. arXiv: 1912.01632 [astro-ph.EP].